Study of Electromagnetic Properties of Zr-Doped $REBa_2Cu_3O_{7-X}$ Coated Conductors Fabricated by Metal Organic Chemical Vapor Deposition over a Wide Range of Temperature & Magnetic Fields

A Thesis

Presented to

the Faculty of the Department of Mechanical Engineering

University of Houston

In Partial Fulfillment

of the Requirements for the Degree

Master of Science

in Materials Engineering

by

Yao Yao

May 2012

Acknowledgements

It is a great honor for me to thank those who made this thesis possible. Firstly, I would like to express my sincerest gratitude to my advisor, Dr. Venkat Selvamanickam, for generously granting me the opportunity to join his research group, effortlessly nurturing my mind, unselfishly sharing his wisdom and constantly encouraging me throughout my work. The sound advice and invaluable support he provided in completing my thesis is greatly appreciated.

My cordial gratefulness also goes to Dr. Yimin Chen for his efforts in preparing all the samples used towards my thesis and his guidance along my work. His knowledge and insights in superconductors helped me through a myriad of difficulties. I want to thank Dr. Goran Majkic for his patience in training me with the high-field system on which all the electromagnetic measurements used in my thesis work were performed. His immense experience and knowledge had been of great value for me. Furthermore, I would like to thank Dr. Changhui Lei and Dr. Eduard Galstyan for the TEM work and Tuo Shi for the XRD data. Without their assistance, there was no way I could finish this thesis.

I am indebted to my colleagues and friends in my group for their help and support in a number of ways: Dr. Senthil Sambandam, T.J. Wainerdi, Scott McKnight, Henri Hansen, David Eldridge, Dr. Yunfei Qiao, Dr. Xuming Xiong, Yue Zhang, Yuhao Liu, Xinwei Cai, Xin Tao, Ying Gao, Jingfu Liu, Ibrahim Kesgin, Yangxin Zhang, Narayan Das Khatri, Albert P. Guevara, Yao Yao, Renjie Wang, Jian Cao, Aarthi Sundaram, Gang Shi and Yuanfei Bi.

I owe my deepest gratitude to my beloved parents Yingguang Yao and Ying Wang, and my fiancée Mei Yang. To them I dedicate this thesis. I also want to address my thanks to my thesis committee members, Dr. Li Sun and Dr. Haleh Ardebili, for their insightful comments and hard questions. Last but not the least, I acknowledge the funding and ICP data from SuperPower Inc. and the support from the U.S. Department of Energy.

Study of Electromagnetic Properties of Zr-Doped $REBa_2Cu_3O_{7-X}$ Coated Conductors Fabricated by Metal Organic Chemical Vapor Deposition over a Wide Range of Temperature & Magnetic Fields

An Abstract

of a

Thesis

Presented to

the Faculty of the Department of Mechanical Engineering

University of Houston

In Partial Fulfillment

of the Requirements for the Degree

Master of Science

in Materials Engineering

by

Yao Yao

May 2012

Abstract

Zr-doped $REBa_2Cu_3O_{7-x}$ (REBCO and RE = Gd, Y in this thesis) coated conductors fabricated by the Metal Organic Chemical Vapor Deposition (MOCVD) method has demonstrated excellent in-field performance at 77K and a low magnetic field in previous research. However, the most important and promising applications of HTS coated conductors requires excellent in-field performance at various cryogenic temperatures between 77K and 20K, or even lower temperatures, with a high external magnetic field.

In this thesis, REBCO coated conductor samples with different Zr contents (0%-15%) fabricated by the MOCVD method were systematically studied in a series of electromagnetic measurements at a wide range of temperatures and fields. Interesting pinning effects of various Zr-doping levels were observed across the temperature and field range. In order to interpret these pinning phenomena, microstructural analysis was done using SEM and TEM methods to reveal the influence of temperature, field and chemical composition on the performance and microstructure of Zr-doped REBCO coated conductors.

Table of contents

Acknowledgements ..... **iv**

Abstract ..... **vii**

Table of contents ..... **viii**

List of Figures ..... **x**

List of Tables ..... **xiii**

Chapter I Introduction **1**

1.1 Introduction to superconductors 1

1.1.1 Discovery of superconductivity 1

1.1.2 Overview of superconductors 2

1.1.3 Development of 1G HTS and 2G HTS 2

1.2 Early fabrication methods of bulk REBCO 6

1.3 Critical current density of REBCO superconductors and flux pinning 7

1.3.1 Reasons for low critical current density of HTS 7

1.3.2 Fabrication of REBCO thin films 10

1.3.3 Enhancing critical current density by flux pinning 16

1.3.4 Flux pinning in REBCO superconductors 20

1.3.5 Low temperature and high magnetic field performance of REBCO coated conductors 27

Chapter II Methodology **30**

2.1 MOCVD system configuration and REBCO thin film deposition 30

2.2 Post-deposition treatments 32

2.3 Electromagnetic measurements 32

2.3.1 Critical Temperature measurement 32

2.3.2 Critical current density measurement 33

Chapter III Results and Discussion 41

3.1 Quality study of REBCO coated conductors 41

3.2 In-field performance of Zr-doped REBCO coated conductors 46

3.2.1 Angular-dependent critical current performance 46

3.2.2 Field-dependent critical current performance 54

3.3 Microstructural study of Zr-doped REBCO superconductors 59

IV Summary and Conclusions 65

References 68

List of Figures

Fig. 1- 1 Schematic illustration of powder-in-tube method (above) and the cross-sectional view of a multi-filamentary Bi-2223 tape (below) (Inada, Iwata et al. 2006). 3

Fig. 1- 2 Orthorhombic perovskite molecular structure of YBCO (http://www.fusione.enea.it/SUPERCOND/ybco.html.en)..... 5

Fig. 1- 3 Dependence of YBCO's superconductivity on its oxygen content 5

Fig. 1- 4 2G HTS coated conductors manufactured by SuperPower Inc. 6

Fig. 1- 5 RABiTS/MOD Fabrication process of 2G HTS coated conductors used by American Superconductor Corporation 12

Fig. 1- 6 Typical tape architecture of coated conductors manufactured by American Superconductor Corporation (without the copper stabilizer layer). 13

Fig. 1- 7 Schematic diagram of IBAD process. 14

Fig. 1- 8 Structure of 2G HTS coated conductor manufactured by SuperPower Inc. 16

Fig. 1- 9 H-T phase diagram of (a) type-I superconductors and (b) type-II superconductors (Emergo 2009). 17

Fig. 1- 10 Structure of a superconducting vortex(Emergo 2009). 17

Fig. 1- 11 Schematic illustration of Lorentz force acting on vortices..... 18

Fig. 1- 12 Three types of pinning centers categorized by their dimensions(Ataru Ichinose 2005). 19

Fig. 1- 13 Pinning effects from deformation of melt-textured YBCO bulk samples. a) 77K angular dependent Jc plots of deformed and undeformed samples; b) 77K angular dependent Jc plot of an isostatically deformed sample (Selvamanickam, Mironova et al. 1993). 21

Fig. 1- 14 Angular dependent Jc of Zr-doped GdYBa2Cu3 O7 coated conductors (Yimin Chen 2011). 22

Fig. 1- 15 SEM photos of surface morphologies of MOCVD-YBCO thin film with different Zr-doping contents: a) undoped, 0 mol%; b) 2.5 mol%; c) 5 mol%; d) 7.5 mol%; e) 10 mol%; f) 20 mol%(Aytug, Paranthaman et al. 2010). 23

Fig. 1- 16 Angular Jc plots at different magnetic fields for a) at grain boundaries and b) within one grain. (Díaz, Mechin et al. 1998). 25

Fig. 1- 17 Angular dependent Jc of MOD-REBCO samples with BZO nanoparticles: a) linear scale; b) logarithmic scale (Awaji, Namba et al. 2010). 26

Fig. 1- 18 J_c performance of MOD-REBCO coated conductors at 65K and 3T with 0% (no dopant added), 25% and 50% Er doping (Holesinger, Civale et al. 2008). 28

Fig. 1- 19 Angular dependent Ic plots at 4.2K and various fields: a) and b) are 4 mm wide samples without BZO nanorods; c) and d) are 4 mm wide samples doped with BZO nanorods (Braccini, Xu et al. 2011). 28

Fig. 2- 1 Schematic diagram of the MOCVD system designed by SuperPower Inc. 31

Fig. 2- 2 Schematic illustration of sample mounting and the four- probe method used during the critical current measurements 34

Fig. 2- 3 An *I-V* curve obtained from a self-field critical current measurement performed at 77K. A detection voltage criterion of 20 μV/cm was used to determine the *Ic* value. 34

Fig. 2- 4 Schematic illustration of the cryostat of the high-field system 36

Fig. 2- 5 Sample stage and accessories of the Ic probe 37

Fig. 2- 6 Photos of samples without (above) and with (below) bridging. 40

Fig. 3- 1 Plot of critical current vs Zr-doping content 42

Fig. 3- 2 θ-2θ scan of Zr-doped REBCO coated conductors 43

Fig. 3- 3 Magnified Plot of θ -2θ scan of Zr-doped REBCO coated conductors 44

Fig. 3- 4 Temperature and Zr-doping content dependence of self-field J_c performance 45

Fig. 3- 5 Temperature and Zr-doping content dependence of in-field performance at a) 77*K* and b) 65*K*. 47

Fig. 3- 6 In-field angular dependence of critical current of Zr-doped REBCO samples at temperatures between 50*K* and 20*K*: (a) 50*K*, 3*T*; (b) 50*K*, 7*T*; (c) 40*K*, 3*T*; (d) 40*K*, 7*T*; (e) 30*K*, 3*T*; (f) 30*K*, 7*T*; (g) 20*K*, 3*T*; (h) 20*K* 7*T*. 49

Fig. 3- 7 Temperature and field dependence of minimum critical currents in angular-dependent measurements of Zr-doped samples: (a) 77*K*; (b) 20*K* to 77*K* at 3*T*; (c) 20 to 50*K* at 7*T*. 51

Fig. 3- 8 Temperature and field dependence of retained current ratio of Zr-doped samples: (a) 1*T*; (b) 3*T*; (c) 7*T*. 52

Fig. 3- 9 Zr-doping content and temperature dependence of the full-width-at- half-maximum of *H*//*ab* peak. The external field was 3*T* (a) and 7*T* (b) respectively. 53

Fig. 3- 10 *H*//*ab* field-dependent critical current and pinning force dependence of Zr-doping content at various temperatures. a) 77*K*; b) 65*K*; c) 50*K*; d) 40*K*; e) 30*K*; f) 20*K*. 55

Fig. 3- 11 *H*//*c* field-dependent critical current and pinning force dependence of Zr-doping content at various temperatures. a) 77*K* ; b) 65*K*; c) 50*K*; d) 40*K*; e) 30*K*; f) 20*K*. 57

Fig. 3- 12 General cross-sectional view TEM photo of a Zr-doped REBCO coated conductor. 60

Fig. 3- 13 TEM planar (upper left) and cross-sectional views of the Zr-doped REBCO thin film with magnified photos of BZO nanorods and RE_2O_3 nanoparticles: a) 7.5% Zr-doped; b) 15% Zr-doped; c) BZO nanorod; d) RE_2O_3 nanoparticle. 61

Fig. 3- 14 Planar RE_2O_3 layer blocking the growth of BZO nanorods by TEM 62

Fig. 3- 15 TEM image and EDS data of the secondary-phases near the buffer layers 63

List of Tables

Table 3- 1 Precursor content ratio information of Zr-doped REBCO thin films 42

Table 3- 2 ICP-MS data of Zr-doped REBCO thin films 44

Chapter I Introduction

1.1 Introduction to superconductors

1.1.1 Discovery of superconductivity

The field of superconductivity commenced in 1911 with Kamerlingh Onnes' observation that the resistance of mercury disappeared after the temperature dropped below 4.15 K in his laboratory located in Leiden University, the Netherlands (Onnes 1911). This temperature, at which a superconductor undergoes a transition from a 'normal state' to a 'superconducting state,' is called the critical temperature, known as T_c. Then he found that the electric current could be propagated in superconducting materials without loss if it was lower than a threshold current density. Above the critical current density J_c, superconductors would revert to their normal state and exhibit an electrical resistance. Onnes observed that the superconducting materials would become normal if the magnetic field they are subjected to reached a certain value, which is known as the critical magnetic field, H_c.

It took almost fifty years to develop a microscopic theory, 'BCS' theory (J. Bardeen 1957), to explain superconductivity as a microscopic effect caused by the "condensation" of electron pairs (Cooper pairs) into a boson-like state. There were also many significant discoveries during these years, including the Meissner effect (W. Meissner 1933) that magnetic flux is excluded from the inside of a superconductor, London equations (F. London 1935) relating electric current to electromagnetic fields in and around a superconductor, Ginzburg-Landau theory (V. Ginzburg 1950) describing the magnetic

vortices and two types of superconductors with different behaviors in an external magnetic field, etc.

1.1.2 **Overview of superconductors**

The discovery of superconductivity triggered a wave of searching for superconductors in different material systems, including metals, alloys and compounds. Until now, over 6000 superconducting materials have been found. However, before 1986, the maximum known critical temperature had risen slowly and only reached 23.2 *K* in Nb_3Ge in 1972. Even so, the discovery of certain Nb alloys with higher T_c and H_c built up the technological foundation to design superconducting magnets that can generate magnetic fields up to 9T during the 1960s (B. Matthias 1954), leading to applications in medical care and high energy physics. The report of a 'possible' critical temperature of 30K in certain La(Ba, Sr)CuO compounds by Bednorz and Muller in 1986 (Bednorz and Muller 1986) was followed by the discovery of YBCO with a T_c about 90 *K* by Wu and Chu a few months later (Wu, Ashburn et al. 1987). A series of new superconductor compounds were steadily discovered. In 1993, T_c above 150 *K* was reported by Chu et al. by applying an ultra-high pressure to Hg-Ba-Ca-Cu-O compounds (Gao, Huang et al. 1993).

1.1.3 **Development of 1G HTS and 2G HTS**

Compared with the limitation of early-found low temperature superconductors (LTS) with T_c no higher than 30 *K*, the discovery of ceramic-based high temperature superconductors (HTS) with T_c well above the boiling point of nitrogen, 77.36 *K*, made several applications feasible, such as power transmission and storage, medical care, high energy physics and military use.

The first generation HTS were made of bismuth-based materials, specifically $Bi_2Sr_2CaCu_2O_{8+x}$ (Bi-2212) and $Bi_2Sr_2Ca_2Cu_3O_{10+x}$ (Bi-2223) by the powder-in-tube method (Ueyama and Ohkura 1996; Schlachter, Frank et al. 2006; Godeke, Denouden et al. 2008), where the superconducting phase is embedded in a non-superconducting matrix, typically silver. After packing the precursor powders into a pure silver tube, the composite was drawn into a wire with a hexagonal cross-sectional shape. Then the wire was cut and restacked into another silver tube to be drawn and flat rolled. The flattened wires were subsequently heat treated at high temperatures to form Bi-2212 or Bi-2223 phase. A schematic illustration of the typical powder-in-tube method and the cross-sectional view of typical multi-filamentary 1G HTS wires made by this technique are shown in Fig. 1-1.

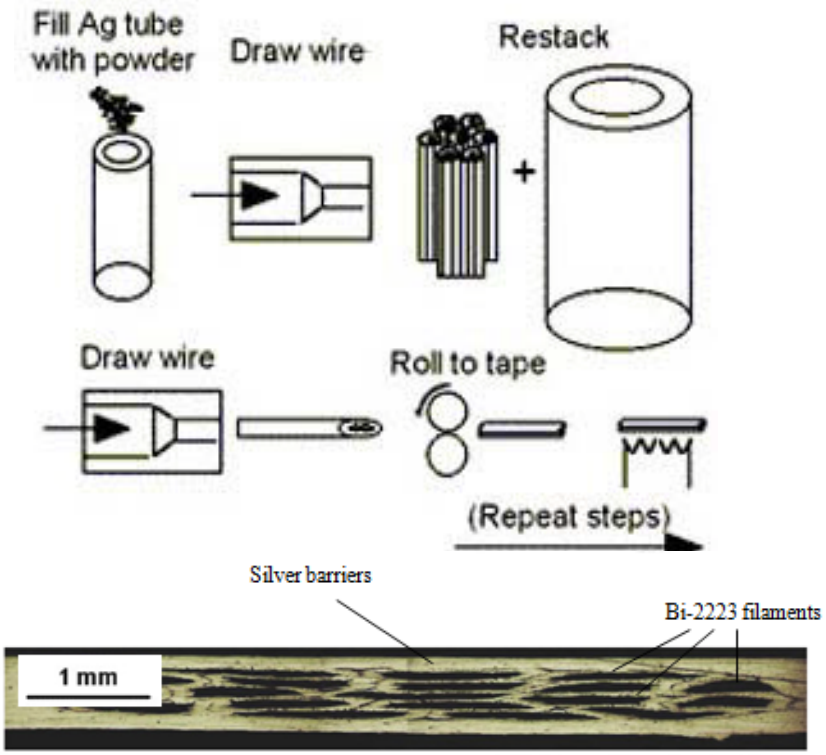

Fig. 1- 1 Schematic illustration of powder-in-tube method (above) and the cross-sectional view of a multi-filamentary Bi-2223 tape (below) (Inada, Iwata et al. 2006).

There are two major drawbacks of 1G HTS which seriously confine its application and development (Sytnikov, Vysotsky et al. 2008):

1) The labor-intensive processing and large amount of expensive metals used for the matrix makes the 1G HTS wire expensive.

2) The irreversibility field, at which the J_c drops to zero, of bismuth-based HTS materials is very low at higher temperatures, which makes 1G HTS highly sensitive to magnetic fields. They lose superconductivity at very low applied fields (~0.2 *T*) at 77 K, which is problematic to the construction of superconducting magnets and other high field applications.

Among all the HTS compounds, rare earth (including Yttrium, Samarium and Gadolinium) based barium copper oxides (REBCO) were gradually chosen as the preferred HTS materials for their excellence in both performance and potential cost. A typical $YBa_2Cu_3O_{7-X}$ (YBCO) lattice has an orthorhombic perovskite structure displayed in Fig. 1-2. As can be seen in the figure, the oxygen and copper atoms are bound together in alternating chains and planes. This layered structure of Cu-O planes is responsible for the superconductivity and the strong anisotropic properties. The oxygen content in the REBCO lattice is very important to their superconductivity as shown in Fig. 1-3. The parameter x in the YBCO formula varies from 0 to 1, determined by the conditions during the subsequent annealing process.

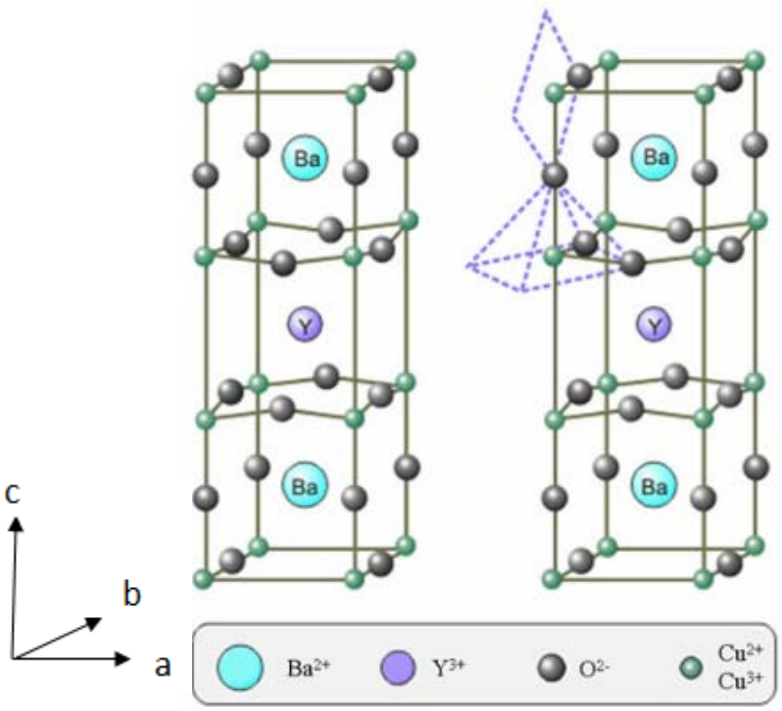

Fig. 1- 2 Orthorhombic perovskite molecular structure of YBCO (http://www.fusione.enea.it/SUPERCOND/ybco.html.en).

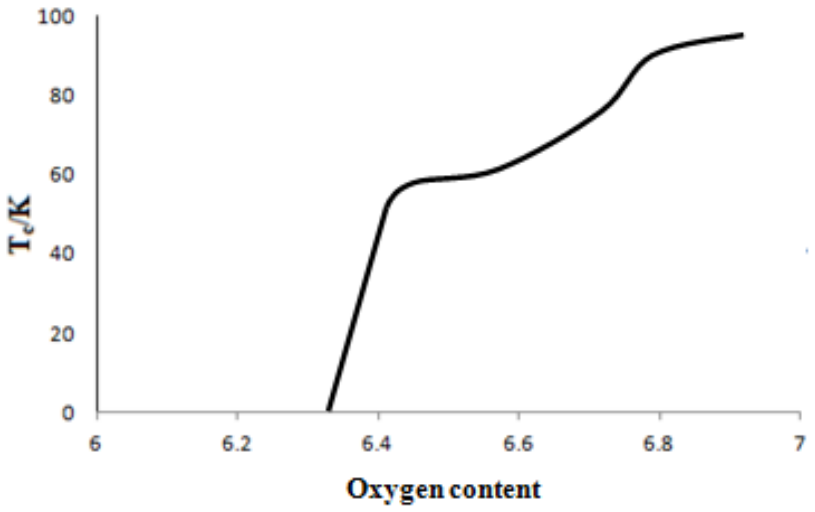

Fig. 1- 3 Dependence of YBCO's superconductivity on its oxygen content.

Gradually, a transition from 1G to 2G HTS occurred among organizations that developed superconducting wires. In the early 2000s, tape-like HTS wires (shown in Fig. 1-4), later designated as 2G HTS, have been developed by several companies and laboratories worldwide, including SuperPower, Fujikura, American Superconductor, Showa, Bruker, Sumitomo, Oak Ridge National Laboratory (ORNL) and Argonne National Laboratory (ANL).

Fig. 1- 4 2G HTS coated conductors manufactured by SuperPower Inc.

1.2 **Early fabrication methods of bulk REBCO**

Due to the high anisotropy of REBCO crystals, it is crucial to control the grain orientation during the fabrication process. Before the development of thin-film-based HTS wires, REBCO was mainly prepared in large-sized bulks using powder sintering, directional solidification, top-seed melt-textured growth or liquid phase processing methods.

Relatively pure YBCO was synthesized by heating a mixture of metal carbonates at temperatures between 1000 to 1300 *K* (Housecroft and Sharpe 2004). Powder mixture of Y_2O_3, $BaCO_3$, and CuO were mixed thoroughly in a proper stoichiometric ratio, according to the following reaction equation:

$$BaCO_3 + Y_2O_3 + CuO + O_2 \rightarrow YBa_2Cu_3O_{7-x} + CO_2. \qquad (1\text{-}1)$$

Ball milling or jet milling was also conducted to reduce the particle size. After calcining, uniaxial pressing, sintering and annealing processes, disk-shaped YBCO samples can be prepared. Due to the weak connectivity at grain boundaries, i.e., weak-link problem, these bulk samples demonstrated very low critical current densities (about 500 A/cm^2 at 77 *K*, 0 *T*) which dropped drastically even at very low applied field ($1A/cm^2$ at 77 *K* 1 *T*) (J. W. Ekin 1987; Schneemeyer, Gyorgy et al. 1987).

1.3 Critical current density of REBCO superconductors and flux pinning

1.3.1 Reasons for low critical current density of HTS

The critical current density, J_c, is one of the most important metrics to evaluate the quality and application prospect of a superconducting material. Thus, the enthusiasm of attaining higher J_c, especially in-field performance, never fades as time goes by. However, one might ask: “Is there a limit of critical current density for a certain superconducting material?,” and the answer is “yes”.

According to the Meissner effect discovered in 1933 (W. Meissner 1933), superconductors are diamagnetic after they have entered the superconducting state because of a supercurrent localized near the surface within a thickness called penetration depth, λ. Most of the superconducting elements in the periodic table fall into the category

of type-I superconductors. In type-I superconductors, when the external magnetic field exceeds a certain value, the surface current density will reach its maximum. Then the superconductor can no longer expel the external magnetic field and lose diamagnetism. Meanwhile, all the high temperature superconductors, alloys and some elements are type-II superconductors. When it comes to the type-II superconductors, the superconductor enters a partially diamagnetic state, called the mixed state. This maximal current density is the depairing current density, J_{cd}. Thus, J_{cd} sets the highest J_c for a superconductor that can be possibly obtained, which is given by equation 1-2:

$$J_{cd} = \frac{H_c}{\lambda} \ , \tag{1-2}$$

where H_c is the critical magnetic field, λ is the penetration depth.

For YBCO at 77*K*, J_{cd} is 240 MA/cm^2. It is about fifty times higher than those demonstrated by the finest YBCO thin films and 3000 times higher for YBCO bulk materials at the same temperature without an outside magnetic field.

In order to understand the cause for this huge difference between the actual J_c values and the J_{cd} value, numerous factors were investigated including stoichiometry, poor connectivity between grains caused by secondary phases, cracks and high-angle grain boundaries, conduction anisotropy, etc. It was found that proper control of microstructure is one of the most effective ways to attain high critical current density of REBCO superconductors. The overall critical current density is determined by whichever is lower of intergrain current density and intragrain current density (Dew-Hughes 2001). The former is a measure of the capability of supercurrent to flow from one grain to an adjacent grain and is controlled by the superconducting coupling between the two grains.

Thus, the intergrain current density will decrease drastically with many of the weak links present at the grain boundaries, which has been confirmed by experiments (Dimos, Chaudhari et al. 1990). As a result, the material that resembles a near single crystal can achieve a high critical current density.

In order to overcome the weak-link problem that plagued in sintered bulk YBCO, Jin et al. (Jin, Tiefel et al. 1988) developed a directional spherulitic growth method during which sintered YBCO bars were heated to 1050~1200°*C* (well above the solidus temperature of 1010°*C*) and then directionally solidified them by cooling in a temperature gradient of not lower than 50°*C/cm* to about 900°*C* followed by an oxygenation heat treatment for 50 *h*. By aligning the orientation of grains, samples made by this technique exhibited a critical current density up to 17 KA/cm^2 at 77 *K* 0 *T* and 4 KA/cm^2 at 77 *K* 1 *T*.

Salama et al. (Salama, Selvamanickam et al. 1989) reported that a critical current density of 75 KA/cm^2 at 77 *K* 0 *T* and that of 8 KA/cm^2 and 3.7 KA/cm^2 in magnetic fields up to 8 *T* and 30 *T* respectively was obtained by employing liquid phase processing method (Ekin, Salama et al. 1991). By very slow cooling of melted YBCO precursor through the peritectic temperature (980°*C*), Y211 and the liquid phase solidify into Y123 superconducting crystal with long grains along the *a-b* plane with minimal cracks and clean grain boundaries without secondary phases. This improved microstructure eliminated the weak-link problem and resulted in more than quadrupling of the highest zero-field critical current density of bulk YBCO at 77 *K* ever reported during that time.

Top-seed melt-textured growth, or Seeding growth, was also an effective way to obtain larger, oriented REBCO bulks (Tang, Yao et al. 2005). Seeds can be non-

superconductive, like MgO, or superconducting, like $REBa_2Cu_3O_{7-x}$ (RE 123) single crystals, or thin films. The top-seed melt-textured growth has been found to be capable of producing highly aligned REBCO bulk samples that demonstrated critical current densities of 20~50 KA/cm^2 at 77 K with no applied magnetic field and 10K A/cm^2 at 77 K 2 T (T Habisreuther 1998).

Bulk REBCO samples provided a good opportunity to study the properties of highly crystalline REBCO superconductors and brought hope to conquer the weak-link problem despite the fact that they were all relatively small (1~10 cm in diameter) and not yet ready for practical applications. Solutions are needed to join REBCO monoliths into various assemblies and shapes for certain applications without sacrificing the critical current density. A number of approaches have been developed and achieved promising results (K. Kimura 1995; P and al. 2000; J. G. Noudem 2001; Lihua Chen 2002; T.A. Prikhna and A. Surzhenko 2003).

1.3.2 **Fabrication of REBCO thin films**

Broad applications of superconducting technology required a new type of HTS processing technique that can be used for fabrication of HTS tapes or wires in large scale with high critical current density especially in the presence of an external magnetic field. Thin film techniques were attempted to make long REBCO superconducting tapes but suffered from weak-link problems at grain boundaries. Dimos et al. (Dimos, Chaudhari et al. 1990) provided the direct evidence that high-angle grain boundaries (>10°) are responsible for the low critical current density and high J_c sensitivity to external magnetic field.

High critical current densities can be achieved in thin film HTS on single crystal substrates, but, it is impractical to produce single crystal substrates in long lengths. Thus, there was a need for feasible techniques for the preparation of polycrystalline substrates that can enable epitaxial growth of high current density HTS thin films. The materials that can be used for epitaxial growth of HTS thin films should have the following properties (Saxena 2010):

1) chemically non-contaminating;

2) good lattice and thermal expansion match with the deposited film;

3) inexpensive.

In the 1990s, there were a number of methods developed for the fabrication of coated conductors around the world, among which the Rolling-Assisted Biaxially-Textured Substrates/Metal Organic deposition (RABiTS/MOD) and Ion Beam Assisted Deposition/Metal Organic Chemical Vapor Deposition (IBAD-MOCVD) have been used to demonstrate long lengths.

RABiTS was first used towards the epitaxial deposition of REBCO thin films on Ni substrates in 1996 at ORNL (A. Goyal 1996). It employs thermomechanical treatment to the base metal, Ni in this case, to obtain a well-developed cube texture followed by the deposition of certain buffer layers for good lattice match with REBCO as well as for chemical and thermal stabilities. American Superconductor's, or AMSC's, approach of producing textured substrates for coated conductors is displayed in Fig. 1-5 (Zhang, Rupich et al. 2007; Rupich, Li et al. 2011). Three buffer layers are deposited on top of a high-purity nickel alloy substrate in the sequence of Y_2O_3, YSZ and CeO_2 by electron

beam deposition (Y_2O_3) and reactive frequency (RF) sputtering (YSZ and CeO_2) in a reel-to-reel system. The crucial MOD-REBCO film is fabricated by a slot-die coating process using trifluoroacetate (TFA)-based precursors (M.W. Rupich 2004). The processed REBCO film is then covered by a thin layer of silver that functions as protection layer and a low resistivity contact. The tape may be slit narrow widths and laminated with a copper stabilizer layer. The typical architecture of RABiTS/MOD coated conductors manufactured by AMSC is shown in Fig. 1-6 (Hawsey and Christen 2006).

AMSC's coated conductors is based on a 0.8 μm thick and 4 *mm* wide REBCO layer deposited by MOD process in length of 200 - 500 *m*, and can carry a critical current about 300 *A* (77 *K*, 0*T*), that is 3.75 MA/cm^2.

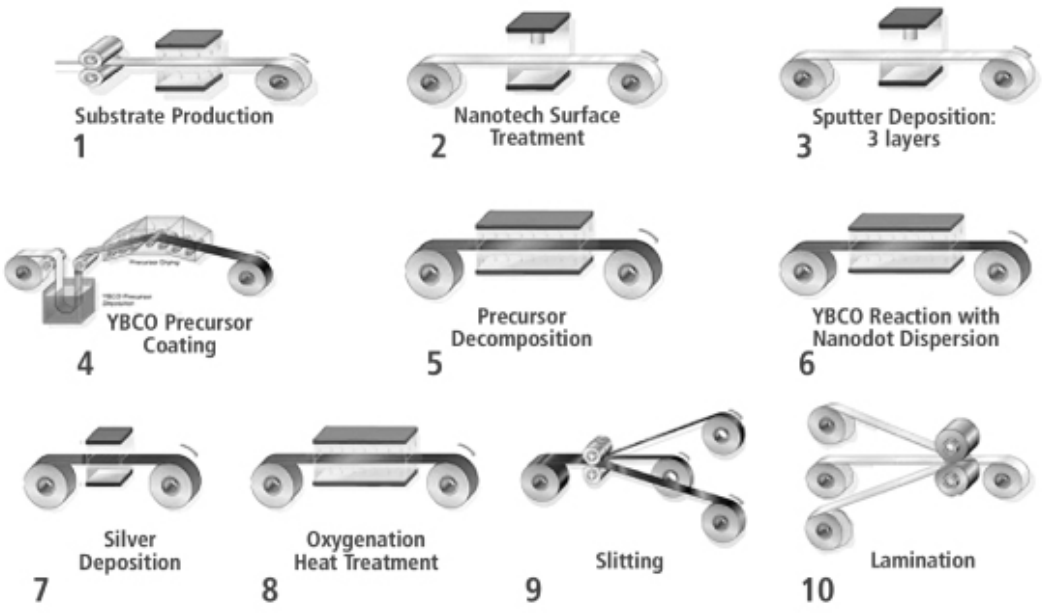

Fig. 1- 5 RABiTS/MOD Fabrication process of 2G HTS coated conductors used by American Superconductor Corporation.

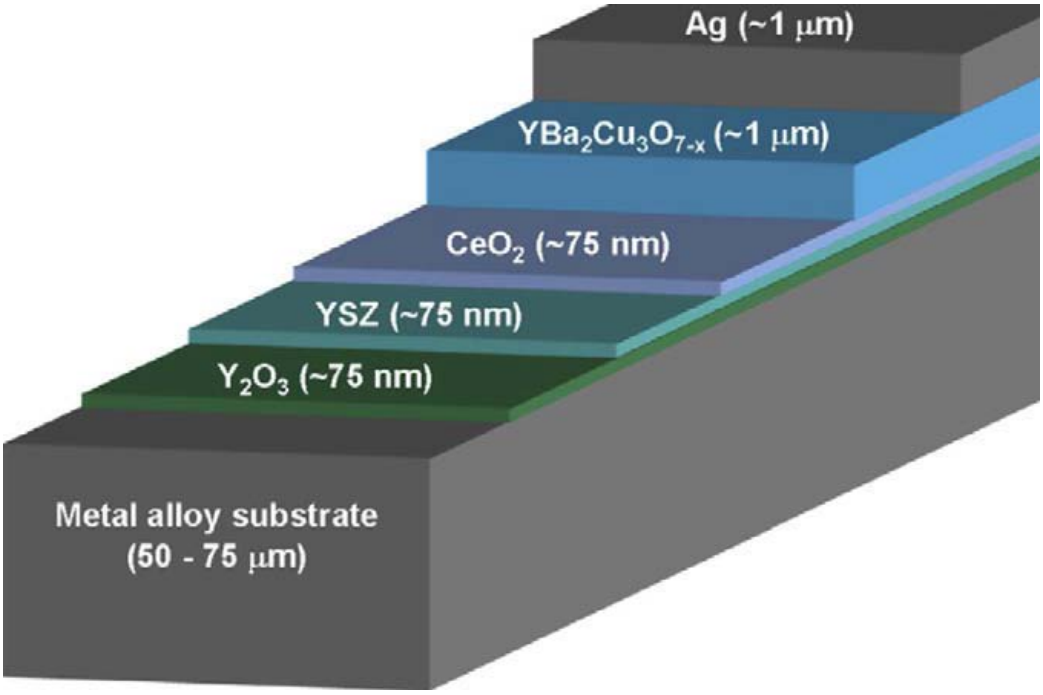

Fig. 1- 6 Typical tape architecture of coated conductors manufactured by American Superconductor Corporation (without the copper stabilizer layer).

SuperPower Inc uses IBAD/MOCVD techniques to fabricate HTS coated conductors. IBAD is a combination of Physical Vapor Deposition (PVD) on a substrate and a simultaneous bombardment of the surface with a low energy ion beam. Fig 1-7 is a schematic illustration of this process.

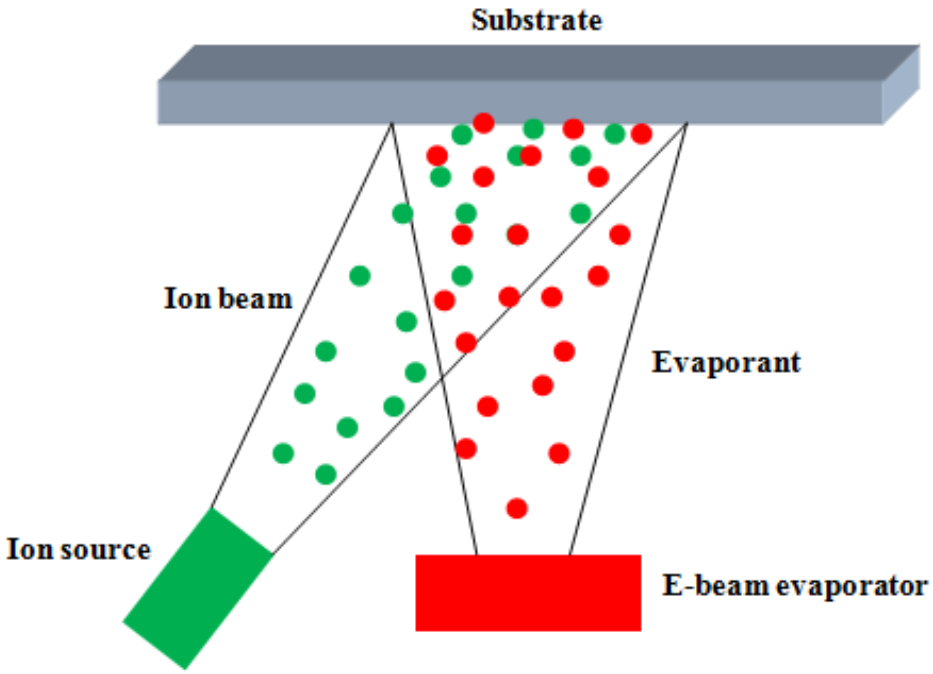

Fig. 1- 7 Schematic diagram of IBAD process.

Iijima et al. (Yasuhiro Iijima 1991) were the first to employ IBAD to produce a biaxially-textured YSZ buffer layer on Hastelloy® substrate, a heat and oxidation resistant superalloy, and deposited a YBCO thin film by Pulsed Laser Deposition (PLD) in 1991. Concurrent energetic particle bombardment used during IBAD can strongly modify the structural properties, including surface morphology, grain orientation and texture of the deposited thin film. Also, the biaxial texture obtained in certain conditions of ion bombardment resulting in a grain-to grain orientation of 10° in *ab* plane and contributed to a J_c of 60 KA/cm^2 (77K 0*T*) and 14 KA/cm^2 (77*K* 0.6*T*). Later, Wu et al. (X. D. Wu 1994) achieved much higher J_c of over 1 MA/cm^2 at 75*K* 0*T* by depositing a thin PLD-CeO_2 buffer layer on top of IBAD-YSZ to obtain a better lattice match with the PLD-YBCO.

In 1988, Berry et al. prepared early YBCO thin films using Metal-Organic Chemical Vapor Deposition (MOCVD) (A. D. Berry 1988). Although these HTS thin films contained plenty of second phases and showed a very wide T_c transition range of $20K$ – $80K$, several researchers worked on developing this technique for HTS thin films during the 1990s (Troger 1992; J. G. Wen 1994; W. Ito 1994; Q. Zhong, P.C. Chou et al. 1995; Shuu'ichirou Yamamoto and Oda 1997). This method has the advantages of large deposition area, fast growth rate, moderate vacuum requirement, external separate precursors and uniform growth on complicated surfaces. Early MOCVD methods used solid precursors which were placed in ovens and sublimed at certain temperatures, then carried by argon gas to the reactor. However, this design gave rise to degradation of precursors, outgrowth of second-phase boulders and irreproducible results, which had seriously hampered the development of MOCVD-REBCO technique. Use of certain adducts led to improvement of the volatility of precursors and suppression of the growth of second phases (Robin A. Gardiner 1994; Zama Hideaki 1994). The use of liquid precursor delivery enabled the use of this technique for coated conductors (D. M. Frigo 1994; Takafumi Kimura 1994; B.C. Richards, S.L. Cook et al. 1995).

MgO was found to be an excellent buffer material for epitaxial growth of thin films on metal substrates in 1997 by Wang et al. (Wang, Do et al. 1997). An optimal texture (2-3 degrees) can be formed by depositing a 10 *nm* thick IBAD-MgO layer that is 100 times thinner than IBAD-YSZ and a much higher critical current density was obtained (J. R. Groves and Stan 2003; Arendt, Foltyn et al. 2004). $LaMnO_3$ (LMO) is used as a lattice matching layer with the superconductor film (Xuming Xiong and Yijie Li 2007).

The tape architecture of the current coated conductor produced by SuperPower is shown in Fig. 1-8.

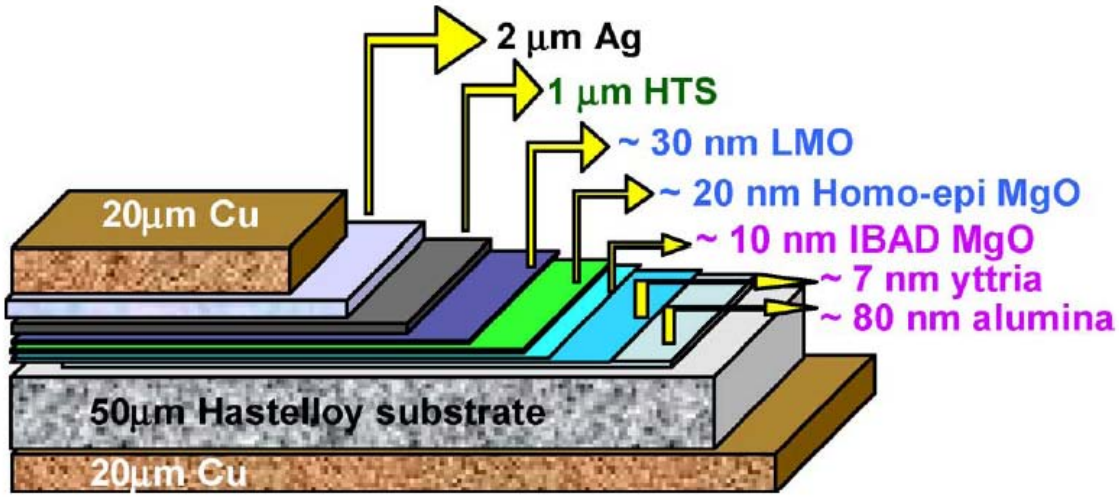

Fig. 1- 8 Structure of 2G HTS coated conductor manufactured by SuperPower Inc.

1.3.3 **Enhancing critical current density by flux pinning**

As mentioned before, type-I and type-II superconductors are different with regard to their magnetic properties. Both of them are characterized by the critical magnetic field, H_c, which is a function of temperature as demonstrated in Fig. 1-9. Particularly in a type-II superconductor, the flux lines can penetrate the material as individual magnetic lines called vortices in the mixed state. As is depicted in Fig. 1-10, the extent to which the magnetic field can penetrate into the superconductor is called penetration depth, denoted as λ. The coherence length ξ is the distance over which the number of Cooper pairs decreases from a maximum value to zero towards the core of the vortices. If the

superconductor is carrying a transport current, the Lorentz force caused by the magnetic field may result in the motion of the flux lines leading to energy dissipation and electrical resistance displayed in Fig. 1-11.

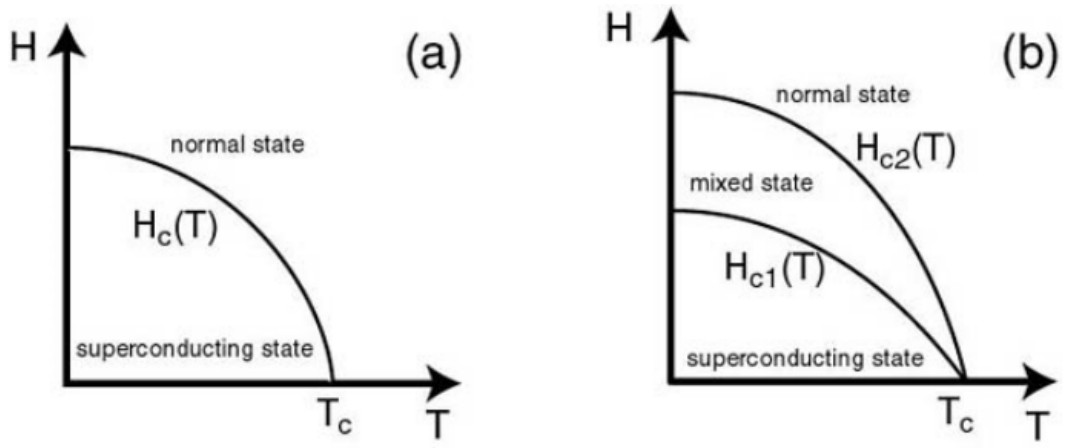

Fig. 1- 9 H-T phase diagram of (a) type-I superconductors and (b) type-II superconductors (Emergo 2009).

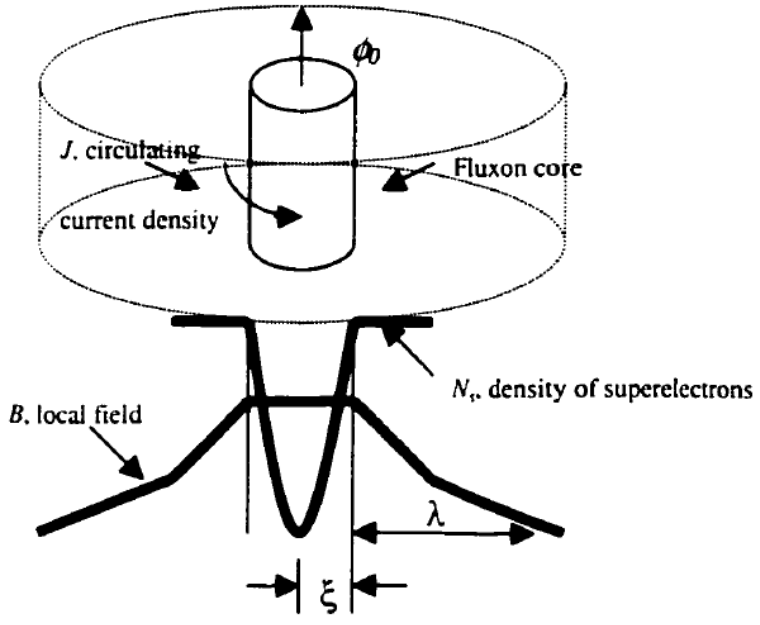

Fig. 1- 10 Structure of a superconducting vortex(Emergo 2009).

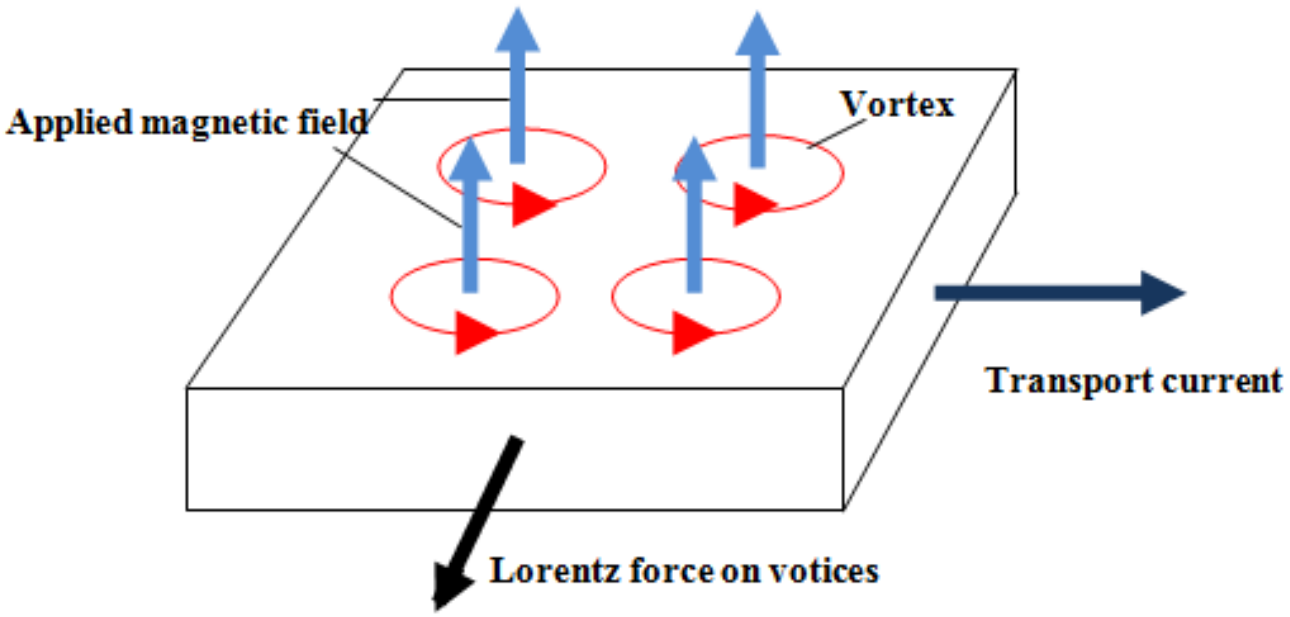

Fig. 1- 11 Schematic illustration of Lorentz force acting on vortices.

Material inhomogeneities and defects in the superconductors can act as pinning centers that can immobilize the flux lines until the Lorentz force reaches a certain critical value. Then the superconductor loses superconductivity and becomes resistive. At this value, the Lorentz force equals to the pinning force and the summation of pinning forces in a unit volume is called the pinning force density, denoted by F_p.

Hence, we have acquired another relation:

$$J_c = \frac{F_p}{B}, \tag{1-3}$$

where J_c is the critical current density, B is the applied magnetic field that is perpendicular to the current.

The inhomogeneities mentioned above in a superconductor are called intrinsic pinning centers, such as crystal structures with alternating strong and less superconducting regions. Intrinsic pinning effect has been seen in REBCO compounds due to their anisotropic layered structures (D.H. Kim 1991).

The defects introduced in superconducting materials during the synthesis and processing including dislocations, impurities, second phases, voids, twin boundaries, etc. are called extrinsic pinning centers and can also produce highly-effective pinning effects. In particular, extrinsic pinning centers in HTS thin films and coated conductors can be classified as one-dimensional pinning (1-D) centers, two-dimensional (2-D) pinning centers and three-dimensional (3-D) pinning centers and are schematically shown in Fig. 1-12 (Ataru Ichinose 2005). One-dimensional pinning centers are linear defects including dislocations, nanorods, and other columnar defects. Two-dimensional pinning centers are planar defects, such as stacking faults, grain boundaries and pancake-like defects. Three-dimensional pinning centers are isotropic nanoparticles or grains of secondary phases dispersed in the matrix. The pinning effects of extrinsic pinning centers are most effective when the size of those is comparable or larger to that of a vortex, 2ξ, about 5~10 *nm* for YBCO at 77*K* (Nick M. Strickland 2009), together with their proper distribution in the superconducting material, which of course can be achieved by various engineering means.

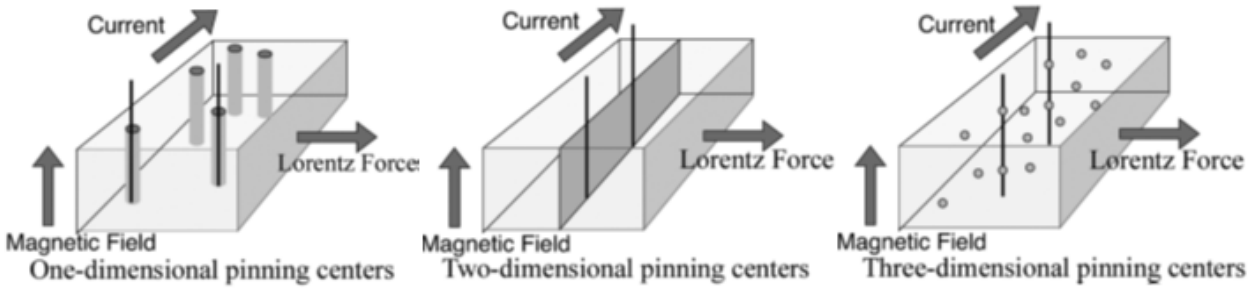

Fig. 1- 12 Three types of pinning centers categorized by their dimensions (Ataru Ichinose 2005).

1.3.4 **Flux pinning in REBCO superconductors**

All REBCO superconductors are type-II superconductors whose critical current densities are determined by the flux pinning mechanism. Considerable efforts have been directed towards the improvement of J_c by enhancing both intrinsic and extrinsic flux pinning effects in REBCO thin films and coated conductors yielding significant J_c increase or dramatic changes in their electromagnetic properties.

The anisotropic structure of a REBCO crystal itself possesses a strong intrinsic pinning mechanism proposed by Tachiki et al. in 1989 (Tachiki and Takahashi 1989). The Cu-O_2 layer, or *ab* plane, can carry much higher supercurrents than the less superconductive *c-axis* direction which separates the *ab* planes and functions as a strong pinning center. This results in the peak effect in the in-field critical current density performance of REBCO HTS materials in which J_c values are much higher when the field is parallel to *ab* plane than that when the field is parallel to c-axis. Some rare earth elements can substitute the Ba position and these substitutes have lower critical magnetic fields than the surrounding matrix phase. When an external magnetic field is increased, these regions will become normal first and act as strong pinning centers (D.H. Kim 1991). Since the oxygen content governs the T_c value of REBCO superconductors, small oxygen-deficiency can cause a drop of T_c in certain areas in the material and contribute significant flux pinning effect (Damling, Seuntjens et al. 1990).

The critical current density of REBCO superconductors can be altered or greatly enhanced by introducing extrinsic or artificial pinning centers (APCs) into the materials. All three types of extrinsic pinning centers have been studied and used both individually and in combinations yielding significant J_c improvements.

Defects in the form of dislocations are typical 1-D APCs in REBCO superconductors. Strong pinning effects of dislocations have been confirmed in the early-made melt-textured REBCO bulk samples (Zhang Pingxiang 1994). Besides the strong intrinsic pinning effects in the direction of *H* parallel to *ab* plane, pinning in other magnetic field orientations was also obtained by introducing dislocations in the material as shown in Fig. 1-13 (Selvamanickam, Mironova et al. 1993). A huge J_c difference in *H*//*c* was observed between the deformed and undeformed samples. Also, additional peaks other than the *H*//*ab* peak appeared in the deformed sample.

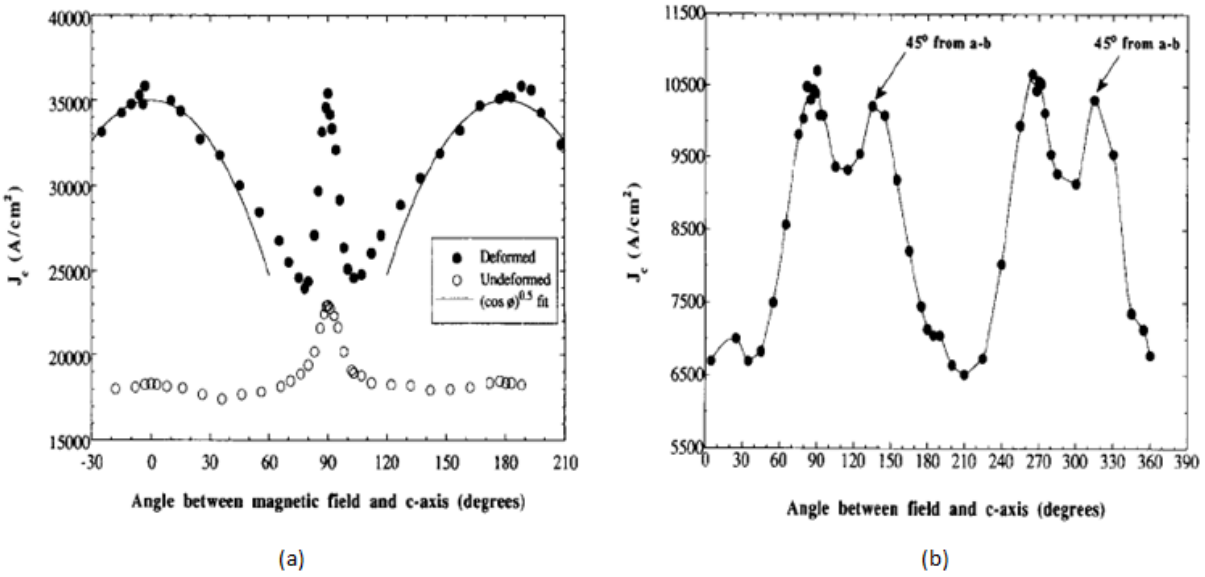

Fig. 1- 13 Pinning effects from deformation of melt-textured YBCO bulk samples. a) 77K angular dependent Jc plots of deformed and undeformed samples; b) 77K angular dependent Jc plot of an isostatically deformed sample (Selvamanickam, Mironova et al. 1993).

Linear defects can also be brought into the REBCO thin films by fabricating Y_2O_3 nano-islands onto the substrates and subsequently growing the superconducting film to gain strong pinning effects along the *c*-axis (Mele, Matsumoto et al. 2008). By introducing second-phase nanorods, such as Y_2O_3 stablized ZrO2 (YSZ), $BaZrO_3$ (BZO)and $BaSnO_3$(BSO), etc. in REBCO thin films using PLD (Haruta, Fujiyoshi et al. 2006; Awaji, Namba et al. 2009; Feldmann, Holesinger et al. 2010), MOD (M.W. Rupich

2004; Zhou, Ghalsasi et al. 2007; Strickland, Long et al. 2008; Fa-Zhu, Hong-Wei et al. 2011), and MOCVD (Chen, Selvamanickam et al. 2009; Aytug, Paranthaman et al. 2010; Yimin Chen 2011), effective *c*-axis correlated pinning centers and substantial J_c enhancement have been obtained. In particular, MOCVD technique has been used to study the compositional effects of RE elements (Gd+Y) and Zr during the synthesis of REBCO coated conductors by precisely and systematically varying the contents of Gd, Y and Zr in the precursors. The optimal Zr-doping content to achieve the best in-field J_c value at 77K was also obtained as shown in Fig. 1-14 (Yimin Chen 2011). As the Zr-addition increases, the shape and size of BZO nanorods has been found to change accordingly as displayed in Fig. 1-15. It was shown that the increase of Zr-addition resulted in the proliferation of secondary phases on the surface (Aytug, Paranthaman et al. 2010).

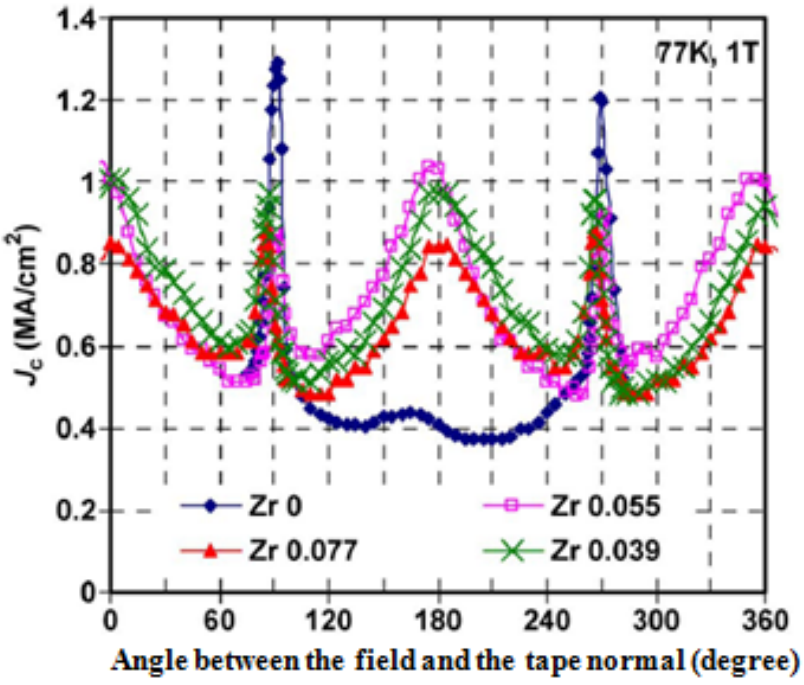

Fig. 1- 14 Angular dependent Jc of Zr-doped GdYBa2Cu3 O7 coated conductors (Yimin Chen 2011).

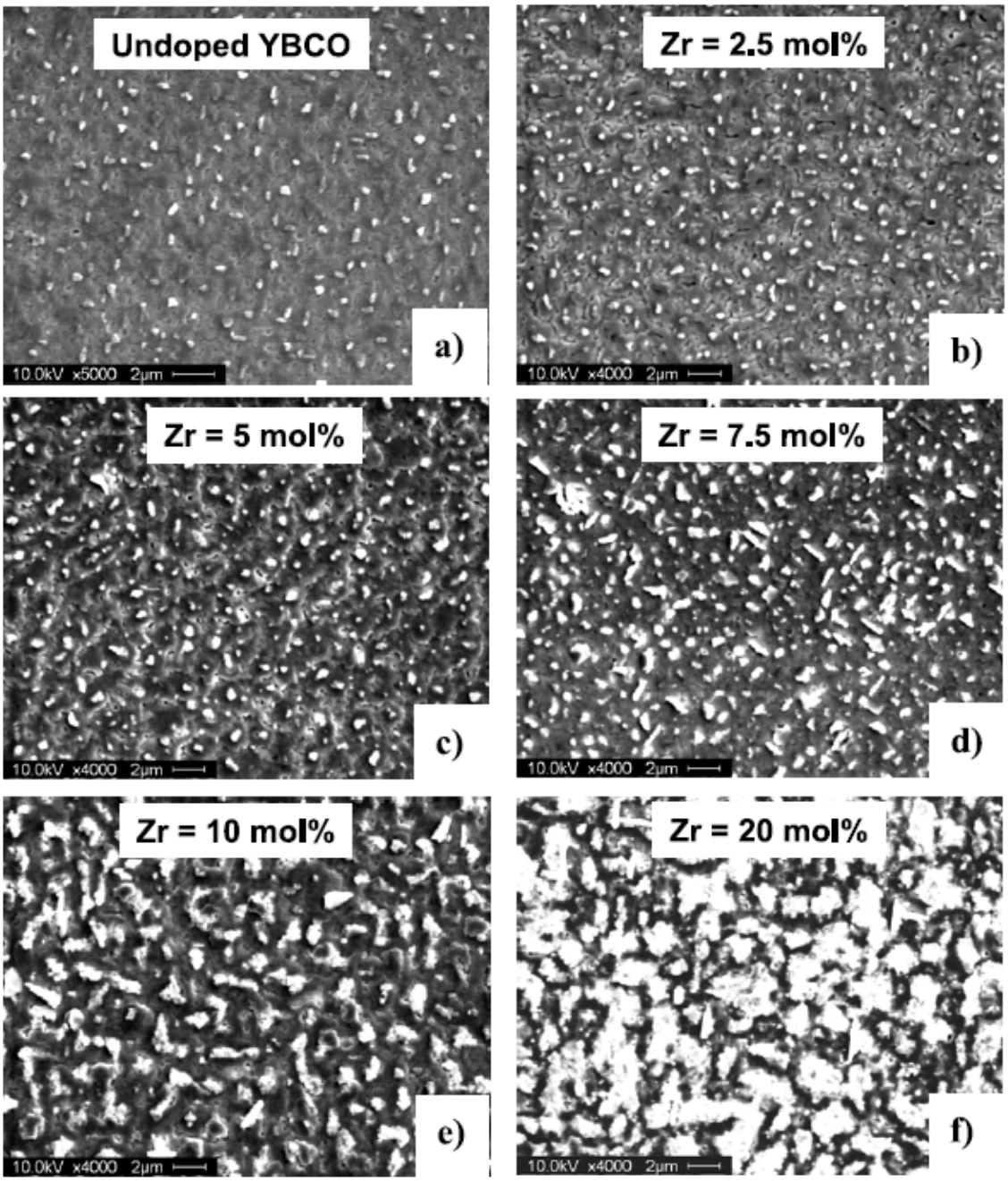

Fig. 1- 15 SEM photos of surface morphologies of MOCVD-YBCO thin film with different Zr-doping contents: a) undoped, 0 mol%; b) 2.5 mol%; c) 5 mol%; d) 7.5 mol%; e) 10 mol%; f) 20 mol%(Aytug, Paranthaman et al. 2010).

An example of 2D APCs is by decomposition of Y124 phase to create evenly spaced extrinsic stacking faults to enhace the in-field critical current density (Kramer 1991). Wang et al. (Wang, Kwon et al. 2008) correlated the in-field J_c performance of high quality YBCO thin films and their varying stacking fault densities controlled by different processing temperatures. A linear relationship was obtained and confirmed that 2D planar defects, like stacking faults, have strong flux pinning effects which can be strengthened by increasing the density of the defects. Similar pinning effects were observed by Diaz et al. in high-pressure DC-sputtered YBCO bicrystal thin films where a broad *H*//*c* peak appeared when the current passes low-angle grain boundaries while no such peak was seen when the current flowed only within the grains as shown in Fig. 1-16 (Díaz, Mechin et al. 1998), where θ is the angle between the tape normal and the magnetic field. The high dislocation density at the low-angle grain boundaries was proposed to result in additional flux pinning effects and could be responsible for the *H*//*c* peaks.

Three-dimensional nanoparticles dispersed in superconducting matrix materials can bring dramatic changes in REBCO's electromagnetic properties which are quite different from those brought by 1D and 2D APCs due to the isotropic characteristic of these nanoparticles. Awaji et al. (Awaji, Namba et al. 2010) reported an isotropic-like in-field behavior caused by the introduction of BZO nanoparticles to MOD-REBCO thin films as shown in Fig. 1-17. The flat angular J_c dependence was ascribed most likely to the strong randomly distributed pinning centers. This phenomenon was especially prominent at low fields and was suppressed as the field was increased. Also, the addition of certain nanoparticles can suppress the superconductivity locally and cause inhomogeneity of superconducting property to produce the pinning effect (Y. Feng 2001; Benazzouz,

Zouaoui et al. 2007). Furthermore, magnetic nanoparticles can also result in excellent pinning effects at various temperatures when doped in optimal contents (Chen-Fong Tsai 2011).

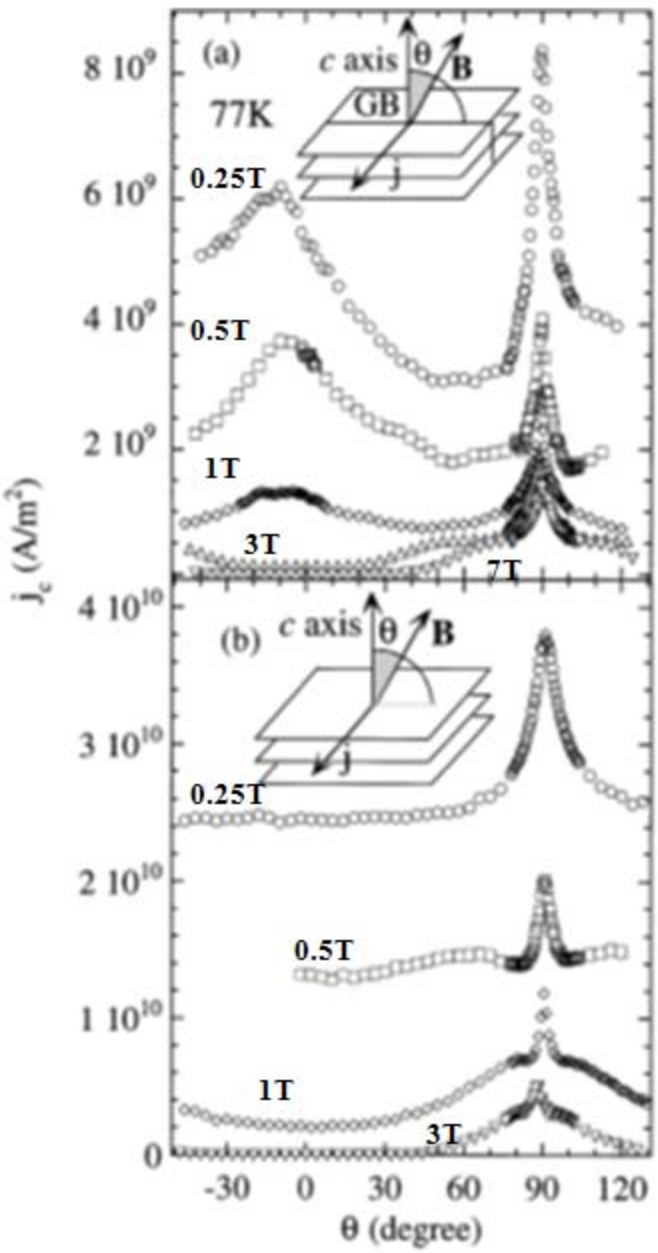

Fig. 1- 16 Angular Jc plots at different magnetic fields for a) at grain boundaries and b) within one grain. (Díaz, Mechin et al. 1998).

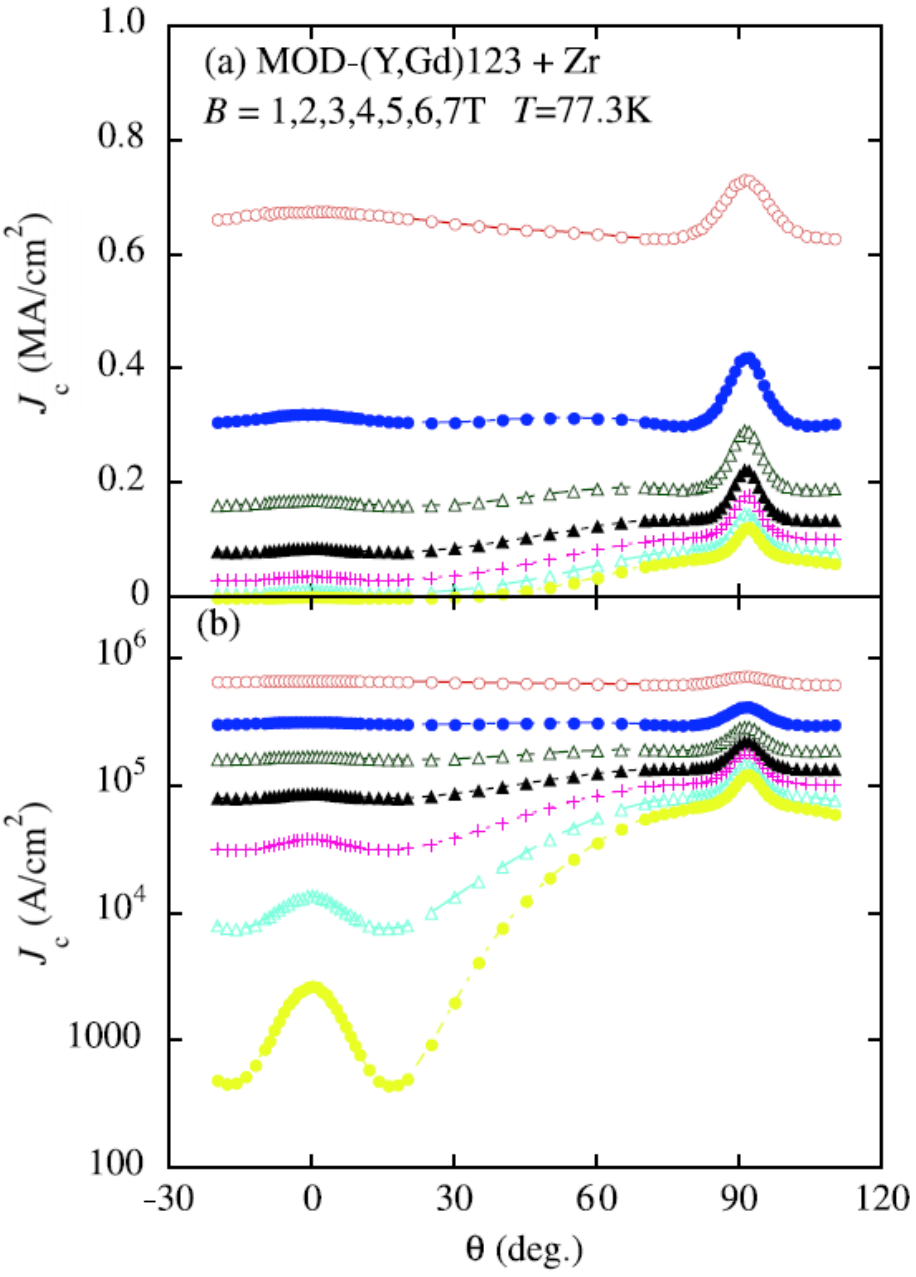

Fig. 1- 17 Angular dependent Jc of MOD-REBCO samples with BZO nanoparticles: a) linear scale; b) logarithmic scale (Awaji, Namba et al. 2010).

1.3.5 **Low temperature and high magnetic field performance of REBCO coated conductors**

The main motivation to develop coated conductors is their superior in-field performance. At intermediate temperatures (50–70 *K*), REBCO coated conductors offer obvious performance advantages over 1G HTS wires for deployment in motors, generators, or other devices at 2–5 *T* magnetic fields. Furthermore, only a single stage cryocooler can be enough for working temperatures above 50*K* (Hawsey and Christen 2006).

Holesinger et al. (Holesinger, Civale et al. 2008) obtained tunable pinning effects of Er-doping in MOD-REBCO coated conductors at 65 *K* and 3*T*. As the content of Er increased up to 50% ($YEr_{0.5}Ba_2Cu_3O_7$), the J_c peak at *H*//*ab* (Fig. 1-18) was found to be lowered drastically, while the J_c in other field orientations was seen to rise significantly. This result was ascribed to the decrease in the density of planar defects and increase in that of splayed defects as the RE element was added to the material.

The electromagnetic properties of coated conductors made using IBAD-MOCVD process with Zr-doping to enhance the flux pinning effects were studied at both liquid nitrogen (77*K*) and liquid helium temperatures (4.2 *K*) at high magnetic fields (up to 31*T*) (Braccini, Xu et al. 2011; Yimin Chen 2011). It was found that BZO nanorods formed by Zr-doping produced much weaker pinning effect at 4.2 *K* (Fig. 1-19) than that produced at 77 *K* (Fig 1-15). Also, a widening tendency of *ab* peak doped with Zr was observed, especially at low magnetic fields. However, no J_c data of Zr-doped REBCO coated conductor samples at intermediate temperatures (20*K*-65*K*) was provided or studied systematically.

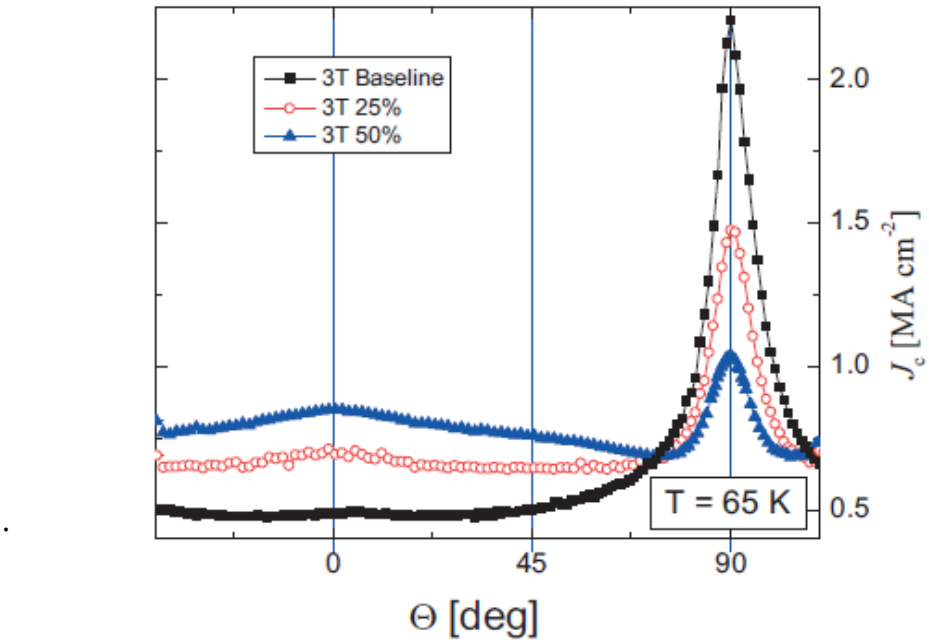

Fig. 1- 18 J_c performance of MOD-REBCO coated conductors at 65K and 3T with 0% (no dopant added), 25% and 50% Er doping (Holesinger, Civale et al. 2008).

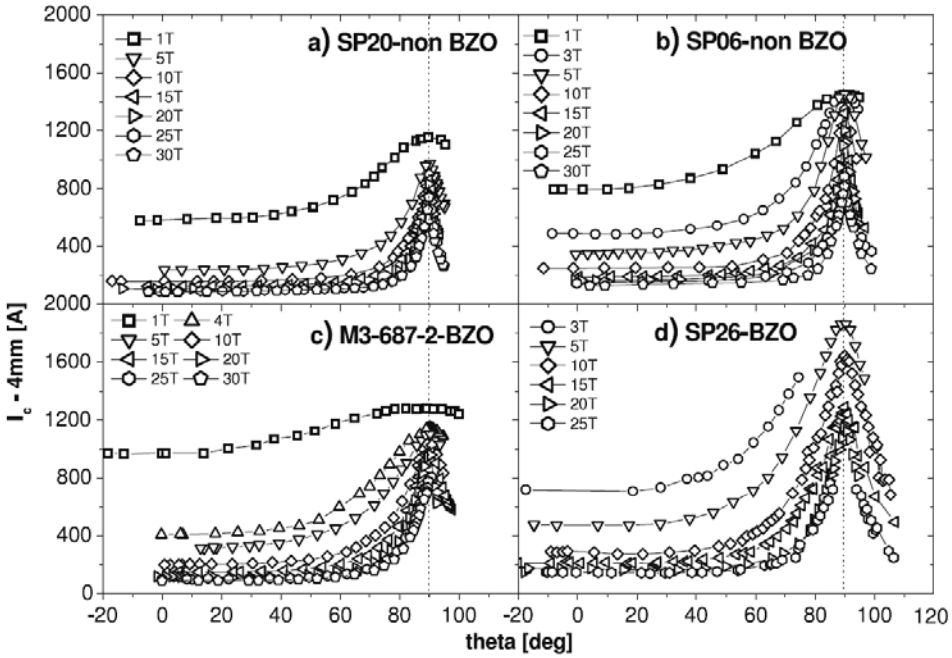

Fig. 1- 19 Angular dependent Ic plots at 4.2K and various fields: a) and b) are 4 mm wide samples without BZO nanorods; c) and d) are 4 mm wide samples doped with BZO nanorods (Braccini, Xu et al. 2011).

Due to the importance of high field and low temperature electromagnetic properties of coated conductors with regard to their applications in high field magnets, generators, motors, transformers, etc., it is necessary to obtain the detailed knowledge of their J_c data over a wide range of temperatures and magnetic fields both to understand the flux pinning mechanisms and to properly construct these superconducting devices.

In this work, REBCO coated conductors fabricated using IBAD-MOCVD technique with various Zr-doping content from 0% to 15% were used for J_c measurements covering a wide temperature range ($77K$ – 20K) at magnetic fields up to $9T$ and over a wide range of angles between the magnetic field and c-axis. The objective is to provide a more complete set of J_c data of Zr-doped REBCO coated conductors and reveal the BZO pinning mechanism at various temperatures and magnetic fields.

Chapter II Methodology

In this chapter, the MOCVD system and its operating procedure used towards the fabrication of REBCO thin films are introduced. Also, the post-deposition treatments including DC sputtering of a silver cap layer and the oxygenation annealing, configurations and operations of the measurement systems and the sample bridging method used in this thesis work are presented.

2.1 **MOCVD system configuration and REBCO thin film deposition**

All the REBCO thin films were fabricated using the cold wall, reel-to-reel and single liquid precursor source MOCVD system, whose schematic configuration is shown in Fig. 2-1. THD precursors (2, 2, 6, 6,-tetramethyl-3, 5-heptanedionate) of Zr, Gd, Y, Ba, and Cu were used as metal organic source materials which were dissolved into an organic solvent, tetrahydrofuran (THF). The standard recipe for a (Gd, Y) BCO thin film is 0.6 (Gd): 0.6 (Y): 2 (Ba): 2.3 (Cu) as the molar ratio and the molar amount of x% dopant used in the process, n_d, is calculated as

$$n_d = \frac{x}{0.6+0.6+2+2.3} n_{total} \ , \qquad (2\text{-}1)$$

where n_{total} is the total molar amount of precursors before doping.

The REBCO thin films were deposited on IBAD-MgO buffered tapes provided by SuperPower Inc. and had the tape architecture shown in Fig. 1-8 with Hastelloy® substrate / Al_2O_3 / Y_2O_3 / IBAD-MgO / MgO / $LaMnO_3$ layers. Buffered tapes were previously spot welded onto Hastelloy® leader tapes and wound to spools that were installed to the reel-to-reel tape handling system. During the deposition process, liquid precursor was pumped into the delivery line and carried by argon gas to the evaporator.

Then the precursor vapor mixed with oxygen was delivered to the reactor consisting of the showerhead and the susceptor to enable the deposition process on the heated buffer tapes that moved at a certain speed. After the REBCO thin film deposition of each recipe group was finished, the precursor vapor would be pumped out and replaced with precursors for the next group.

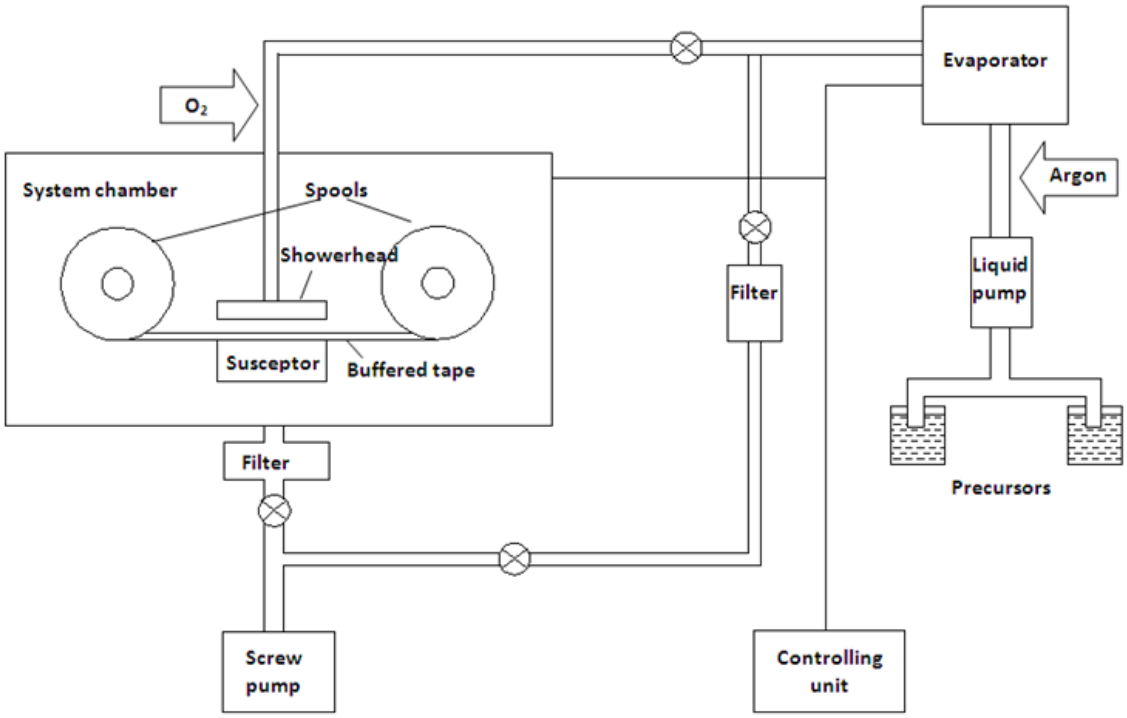

Fig. 2- 1 Schematic diagram of the MOCVD system designed by SuperPower Inc.

2.2 **Post-deposition treatments**

After the deposition process, REBCO samples were cut off from the leader tapes and sputtered with a layer of silver in a DC sputtering system. The silver cap layer provides a means of good electrical contact and excellent solderability. The thickness of the silver layer is about 1 μm determined by the power output and deposition time.

An oxygenation heat treatment was applied to replenish the oxygen in REBCO lost during the MOCVD and silver sputtering processes. The sputtered REBCO coated conductor samples placed in a horizontal tube furnace were oxygenated at 500°C for 10h in flowing oxygen. The ramp up and ramp down rates were 200°C/h and 180°C/h, respectively. After the samples were cooled to room temperature, they were taken out of the furnace and used for the following electromagnetic measurements and materials characterization.

2.3 **Electromagnetic measurements**

There were two kinds of electromagnetic measurements included in this thesis work to determine the performance of the REBCO coated conductors, namely critical temperature measurement and critical current density measurement. A description of these electromagnetic measurements is provided in this section.

2.3.1 **Critical Temperature measurement**

The Meissner effect exhibited by superconductors below critical temperatures was applied to design the critical temperature measurement system. During the measurement, a sample was placed between an excitation coil that generated a weak magnetic field and a pickup coil. Then the sample was cooled to around 77.4 K, the boiling point of liquid

nitrogen, and slowly warmed up. Once the critical temperature was reached, the sample could no longer shield the field produced by the excitation coil and the pickup coil would generate an induced field. The sample temperature and the induced field intensity of the pickup coil were monitored and recorded by a computer via the on-board temperature sensor and a lock-in amplifier respectively.

2.3.2 **Critical current density measurement**

The critical current density data was generated during the electromagnetic measurements, including self-field I_c measurement and in-field I_c measurement. A four-probe method was used in all the critical current measurements. All the contacts between voltage detecting wires and samples, samples and silver current leads, silver current leads and the copper current tabs shown in Fig. 2-2 were made with indium solder. Indium melts at 156 $°C$ which is low enough to protect samples from the potential damage caused by heat. The detection voltage criterion used to determine the critical current was 20 microvolt per centimeter of spacing between voltage detection contacts. During each measurement, a direct current (DC) generated by the power supply was carried by the sample. Until the critical current is reached, no voltage drop is observed. After the current reaches the critical value, the sample becomes resistive and shows an Ohmic behavior. The current at the detection voltage criterion is defined as the critical current. A typical Current versus Voltage (I-V) curve of I_c measurement is shown in Fig. 2-3. The configurations of measurement systems, measurement operating procedures, problems frequently met during measurements and respective solutions are discussed in detail next.

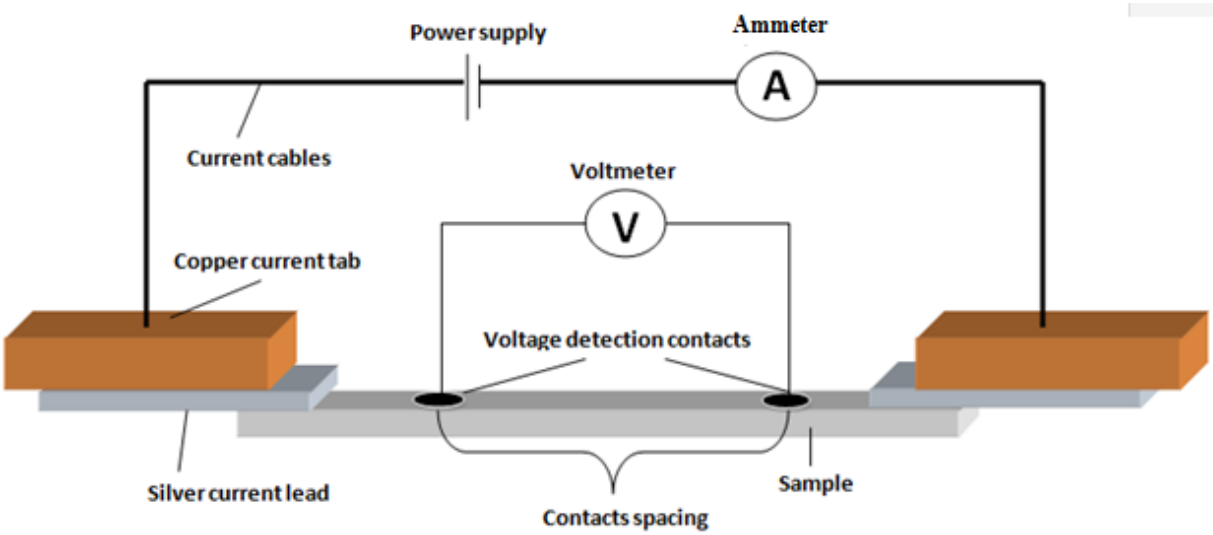

Fig. 2- 2 Schematic illustration of sample mounting and the four- probe method used during the critical current measurements.

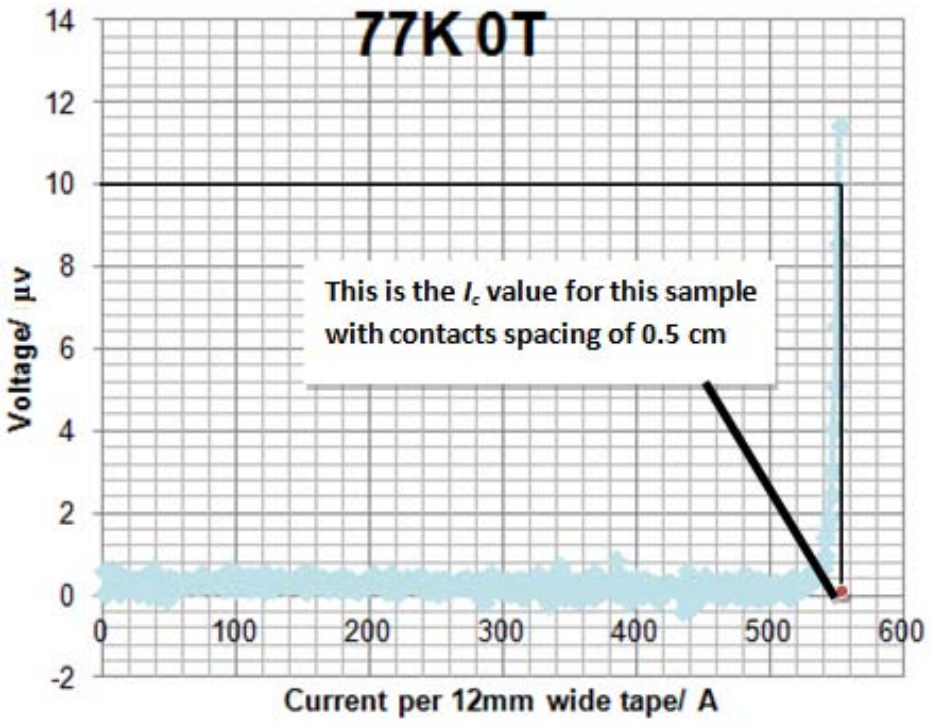

Fig. 2- 3 An *I-V* curve obtained from a self-field critical current measurement performed at 77K. A detection voltage criterion of 20 µV/cm was used to determine the *Ic* value.

Self-field I_c measurement

Self-field I_c measurements were performed without an external magnetic field and are very useful for quality control and preliminary screening of REBCO samples. The self-field I_c measurement system consists of a sample stage with current cables and a computer hooked up with a power supply and a Keithley multimeter. After mounting a sample on the stage and immersing the stage into a Dewar containing liquid nitrogen, a LabVIEW program preloaded in the computer was used to perform the measurement very quickly.

In-field I_c measurement

The in-field critical current measurements were performed with a custom-designed cryogen-free 9 *Tesla* electromagnetic characterization system by Cryogenic Ltd, denoted as the high-field system for convenience. This high-field system enabled programmable angular and field dependent measurements at various temperatures as low as 4 K and magnetic field up to 9 T with no need of feeding supplying cryogen (usually helium and nitrogen) to the cryostat.

The high-field system is mainly made up of three parts: cryostat, I_c probe and controlling system. The cryostat displayed schematically in Fig. 2-4 is composed of an aluminum alloy vacuum cryostat, two compressors and a gas reservoir bag. The vacuum cryostat contains the 9 T magnet, cryocoolers, inner circulation vessels and multiple resistive heaters. The 9 T superconducting magnet sits in the center of the cryostat. Two Gifford McMahon cryocoolers manufactured by Sumitomo Cryogenics of America Inc. were incorporated to the high-field system. One is dedicated for cooling the magnet while

the other is used solely for cooling the probe. The strong cooling power generated by the cryocoolers can condense the gaseous helium into liquid helium that circulates in the vessels and using resistive heaters, the inner temperature of the cryostat is maintained. Thermocouples are located throughout the cryostat and connected to the control system to monitor the temperatures of various internal components during the operations. The outer case of the cryostat has ports for the compressors, magnet current leads, magnet protection leads, instrumentation, evacuation, overpressure, etc.

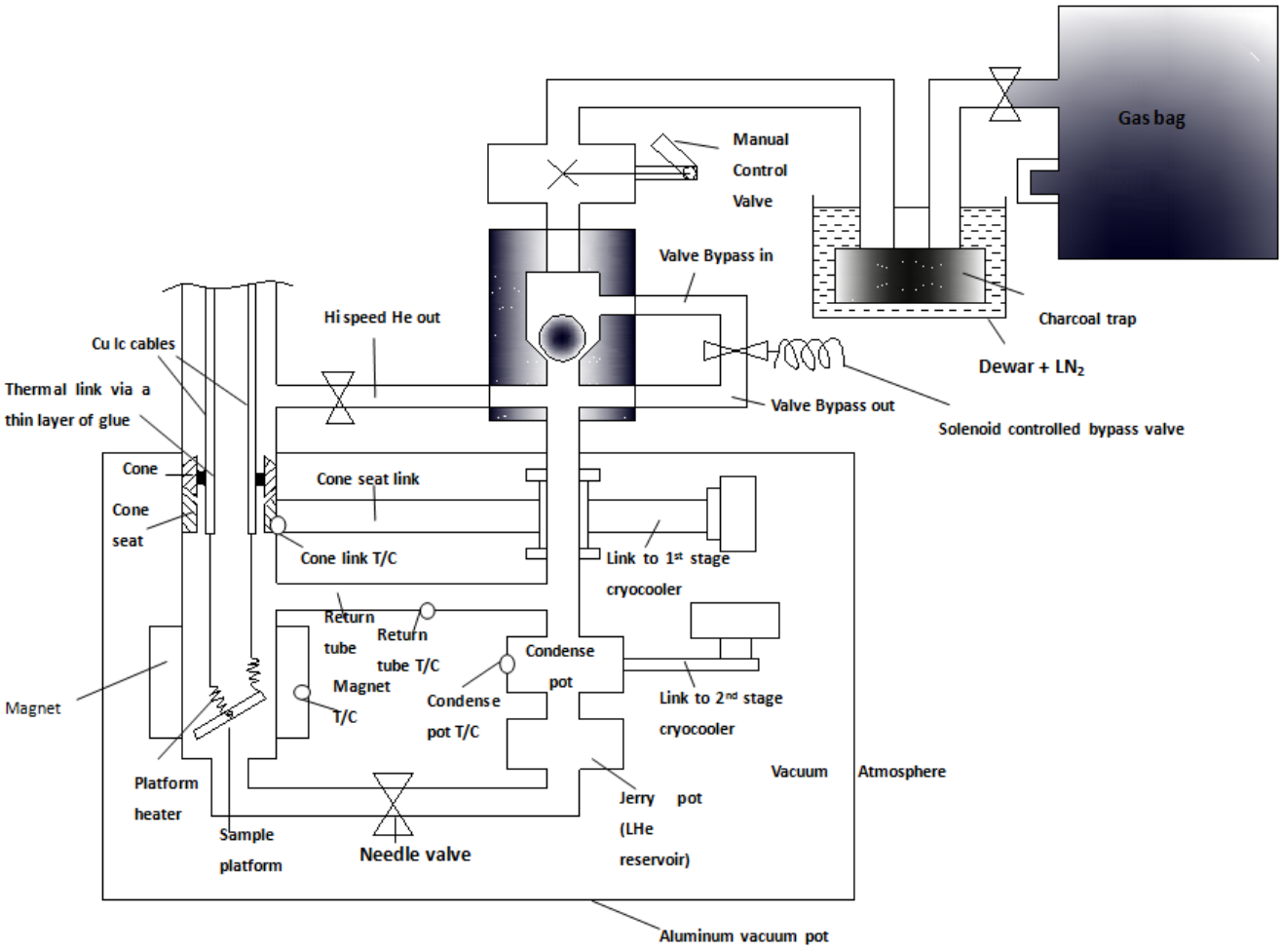

Fig. 2- 4 Schematic illustration of the cryostat of the high-field system.

A high current sample rotation I_c probe is used with the high-field system. The I_c probe is integrated with a motorized rotating sample platform, 600 *A* current leads, a Hall sensor and a sample thermometer. The motorized rotator on top of the probe is manipulated by the control system and provides a moving range of 200 *degrees* for the sample platform shown in Fig. 2-5.

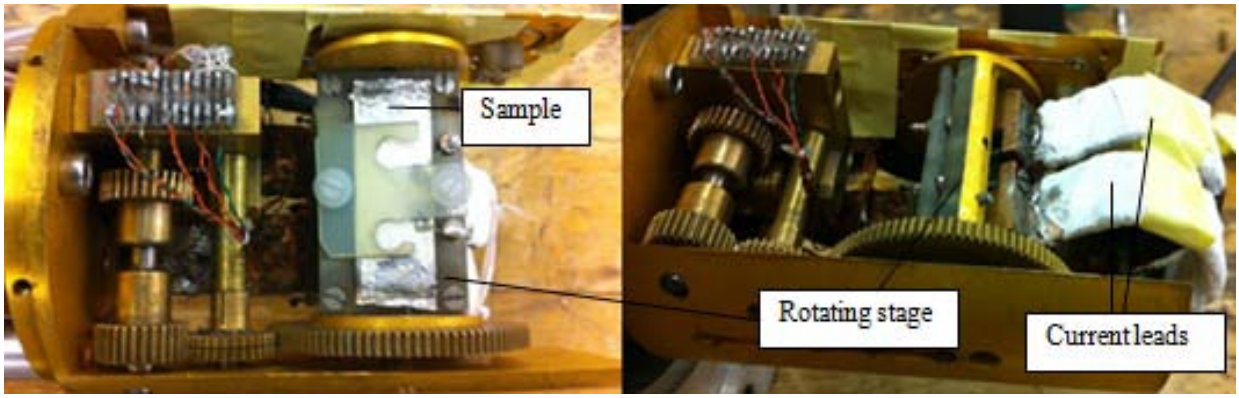

Fig. 2- 5 Sample stage and accessories of the Ic probe.

The control system was made up of a computer and several electronic instruments, including a Keithley Scanner 7200, a Keithley Nanovoltmeter 2182, a Lakeshore 336 Temperature controller, a SMS-120C-4Q magnet power supply and a 600 A Power supply. A LabVIEW program was used to execute all the monitoring and control operations of the high-field system. A ‘sequence’ file could be created and loaded to the program. Then it automatically carried out a series of I_c measurements in different angle, temperature and magnetic field conditions appointed in the ‘sequence’ file.

The operating procedure of the high-field system is as follows:

1) Weld the sample onto the sample platform and solder the voltage detecting wires on the sample with a Weller welding station and indium solder.

2) Mount the probe to the system and pump down the airlock in the probe to the pressure below 1 *mTorr*.

3) Lower the sample platform to the cryostat and watch the sample temperature.

4) After the sample temperature reached the desired value, load the sequence file created earlier and start the measurements.

5) Once all the measurements are finished, slowly raise the sample stage and warm it up to the room temperature.

6) Remove the probe from the system and change the sample to move on to the next measurement.

Sample bridging

One of the biggest issues with the I_c measurements was the sample burnout problem. A standard REBCO coated conductor sample used in this thesis work was 12 *mm* in width and the thickness of the REBCO thin film was about 0.8 to 1.1 μm. Such a tape could typically carry a self-field critical current of 300 - 400 *A* at 77*K*. Once the sample became resistive with this high transport current, a significant joule heating is generated which could result in a drastic local temperature rise, cause a burnout and damage the sample permanently. Sample burnout problem frequently occurs during self-field I_c measurements at 77*K*. It can be probably ascribed to the poor thermal conductivity of the

nitrogen bubbles around the sample that can inhibit the dissipation of joule heat generated during the measurement. No sample burnout was ever seen in the high-field system because of its strong cooling power and excellent temperature stabilizing capability. Since both the self-field measurement system and the high-field system were equipped with 600 *A* maximum current output power supplies, critical currents higher than 600 *A* could not be measured using a full-width, i.e., 12 mm wide sample, at lower temperatures.

In order to overcome the sample burnout problem and enable critical current measurements at low temperatures, a sample bridging method to proportionally reduce the transport current was developed. The procedure for the sample bridging method is as follows:

1) A bridge of 1~2 *mm* in width is patterned on a standard sample with Kapton® tapes.

2) The patterned sample is dipped into the silver etching solution (40% ammonium hydroxide + 40% hydrogen peroxide + 20 *vol%* distilled water) with tweezers until the silver layer not covered by Kapton® tapes was etched away.

3) After rinsing the sample with flowing tap water, it is dipped into the REBCO etching solution (10 *vol%* nitric acid) for about 10 *seconds*. Then wait for the remaining black REBCO layer to disappear. This can prevent over-etching that damages the bridge.

4) The sample is rinsed with flowing water and all the Kapton® tapes are removed carefully.

Samples with and without bridging are displayed in Fig. 2-6 for comparison. Sample bridging successfully solved the sample burnout problem for self-field I_c measurement and enabled critical current measurements with the existing hardware at temperatures as low as 4.2 *K*. The I_c value of the 12 mm wide tape can be calculated using

$$I_c = \frac{w_0}{w} I_{c,b} \ , \qquad (2\text{-}2)$$

where w_0 is the width of a standard sample, 12 *mm*, and w is the width of the bridge measured with an optical microscope, $I_{c,b}$ is the critical current of a bridged sample.

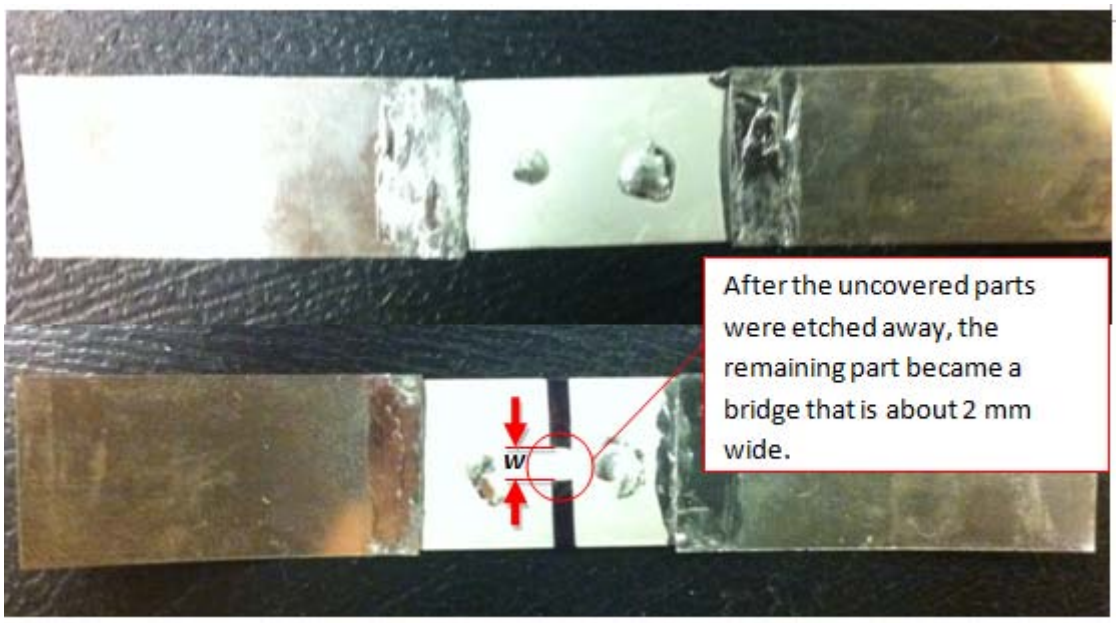

Fig. 2- 6 Photos of samples without (above) and with (below) bridging.

Chapter III Results and Discussion

The pinning effects of self-assembled BZO nanorods and RE_2O_3 precipitates in MOCVD-REBCO coated conductors at 77K and low magnetic field have been systematically studied previously (Chen, Selvamanickam et al. 2009). However, the conclusions with regard to the pinning mechanism of BZO and RE_2O_3 obtained so far are very limited and might not be applicable in a wide range of temperature and field conditions. Since most of the applications of REBCO coated conductors involve high magnetic fields at various cryogenic temperatures, the in-field performance of these superconducting wires in such conditions is very critical. In this chapter, a systematic performance study of REBCO coated conductors at low temperatures and high magnetic fields are presented.

3.1 Quality study of REBCO coated conductors

The precursor molar ratio of Gd: Y: Ba: Cu (0.6: 0.6: 2: 2.3), the low growth rate condition (0.133 $\mu m/min$) and the susceptor temperature (972°C) applied in preparing the REBCO thin films for this thesis work were previously optimized (Chen, Selvamanickam et al. 2009). The precursor composition of Zr dopant is shown in Table 3-1. The thickness of the REBCO thin films fabricated for this work is ~ 0.8 μm. The relationship between the critical temperature and the Zr content of REBCO coated conductors is displayed in Fig. 3-1. As the Zr dopant increased in the REBCO thin films, the Tc was found to drop accordingly.

Table 3- 1 Precursor content ratio information of Zr-doped REBCO thin films.

Zr%	Precursor content ratio (Zr: Gd:Y:Ba:Cu)
0%	0: 0.6: 0.6: 2: 2.3
5%	0.05: 0.6: 0.6: 2: 2.3
7.50%	0.075: 0.6: 0.6: 2: 2.3
10%	0.1: 0.6: 0.6: 2: 2.3
15%	0.15: 0.6: 0.6: 2: 2.3

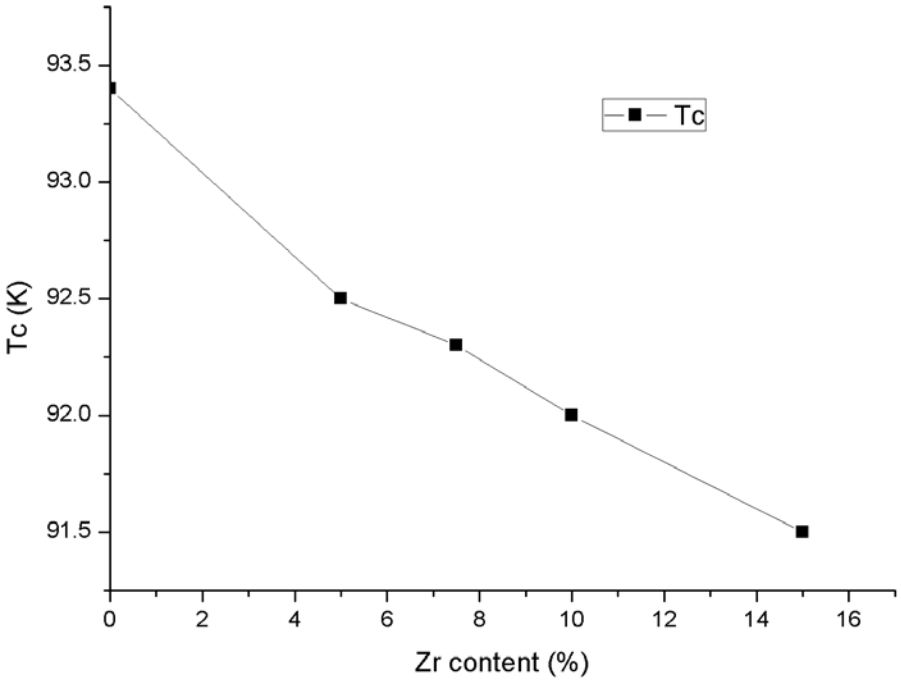

Fig. 3- 1 Plot of critical current vs Zr-doping content.

Fig. 3-2 shows the θ -2θ XRD diffraction patterns for the Zr-doped REBCO coated conductors (Shi 2011). It is worth noting that a good epitaxial, *c*-axis well-oriented

REBCO phase shows all major diffraction peaks denoted as (*0 0 l*) reflections. In addition to those (*0 0 l*) peaks, some weaker peaks were also observed in Fig. 3-2, such as (400) and (200) peaks for RE_2O_3 and BZO structures. Self-assembled BZO nanorods have been observed along *c*-axis (out-of-plane) with diameters between 5 ~ 10 *nm* (Chen, Selvamanickam et al. 2009; Fazhu Ding 2012). This has been confirmed in the TEM study of our samples and are discussed later in this chapter. Furthermore, the (200) peaks at 43.5° from the θ-2θ scan shown in Fig. 3-3 increases with the Zr content and the other peak next to the (200) peak shows the perovkite buffer layer, i.e., MgO.

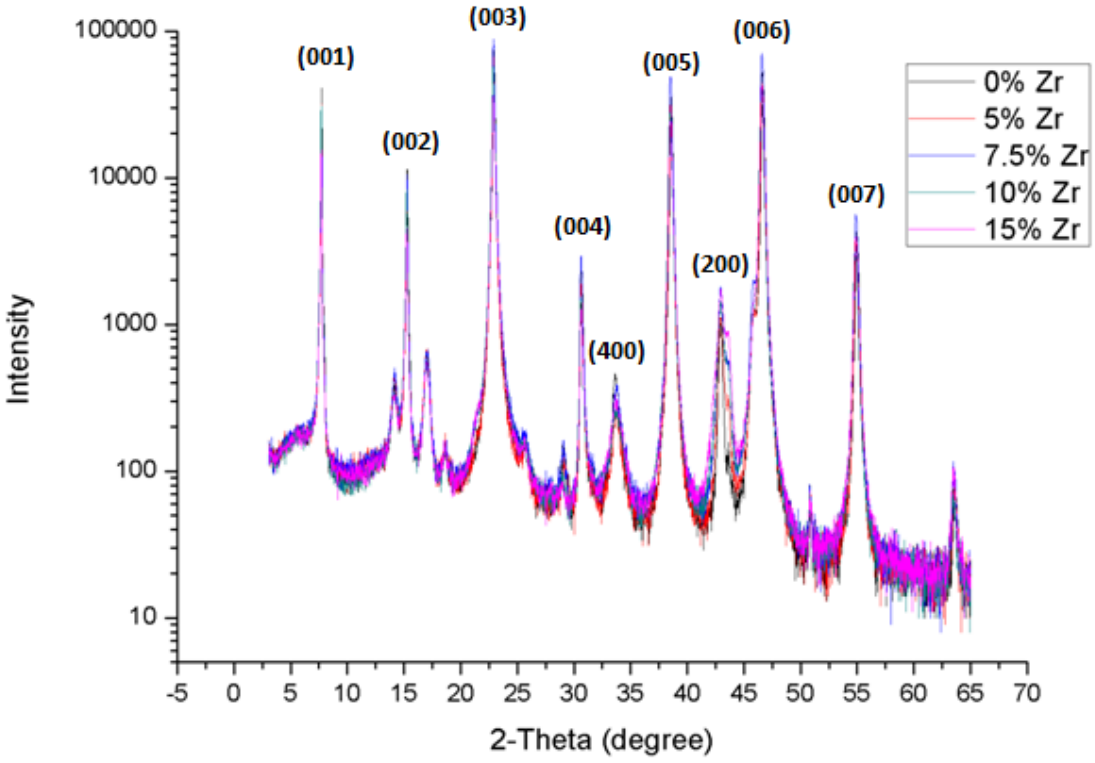

Fig. 3- 2 θ-2θ scan of Zr-doped REBCO coated conductors.

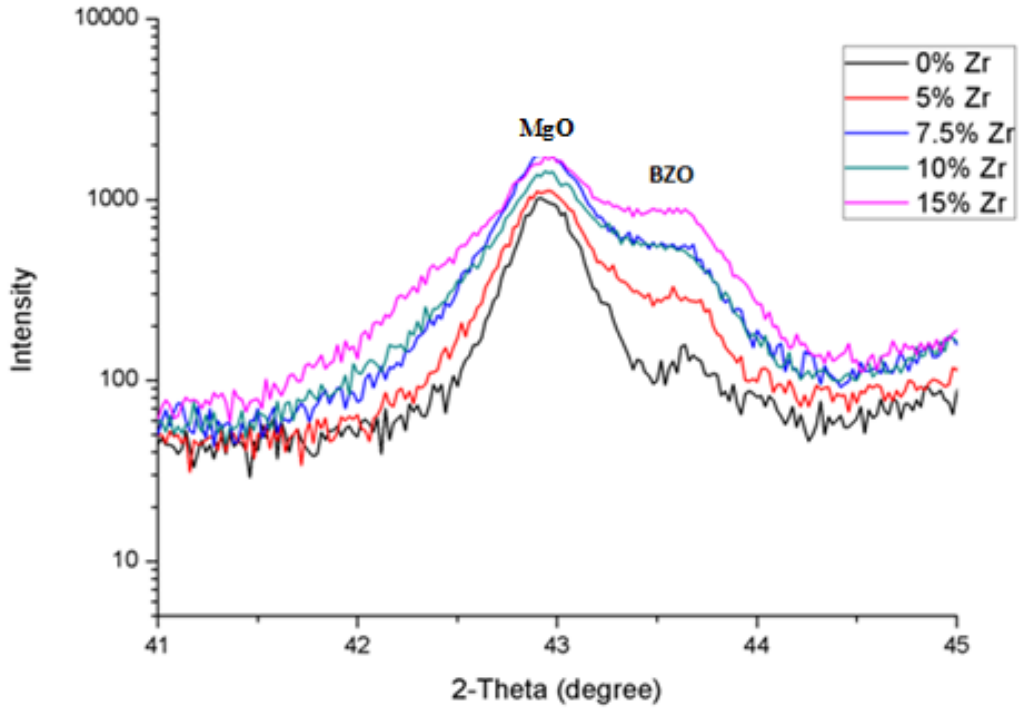

Fig. 3- 3 Magnified Plot of θ -2θ scan of Zr-doped REBCO coated conductors.

Inductively coupled plasma - mass spectrometry (ICP-MS) data for Zr-doped REBCO thin films is shown in Table 3-2. As the Zr content in the precursor is increased, the molar ratio of Zr incorporated into the films increased as well, which agreed with the change of BZO peak intensity observed in the θ -2θ XRD data.

Table 3- 2 ICP-MS data of Zr-doped REBCO thin films

Zr in the precursor (mol %)	0	5	7.5	10	15
Zr in the films (mol %)	0	3.6	5.4	7.9	12.2

The self-field critical current values, I_c, of REBCO samples with different Zr contents at temperatures between 77*K* to 20*K* are plotted in Fig. 3-4. All critical current data of REBCO coated conductors studied in this thesis work was normalized to the I_c of the standard 12 *mm* wide tape as calculated in equation 2-2. As the Zr content increased in the REBCO thin films, the self-field I_c decreased above 65 *K*, but a rise of I_c in the 7.5% Zr sample as the temperature went lower was seen. However, an accelerating drop of I_c as the Zr-content went above 7.5% was seen at all temperatures.

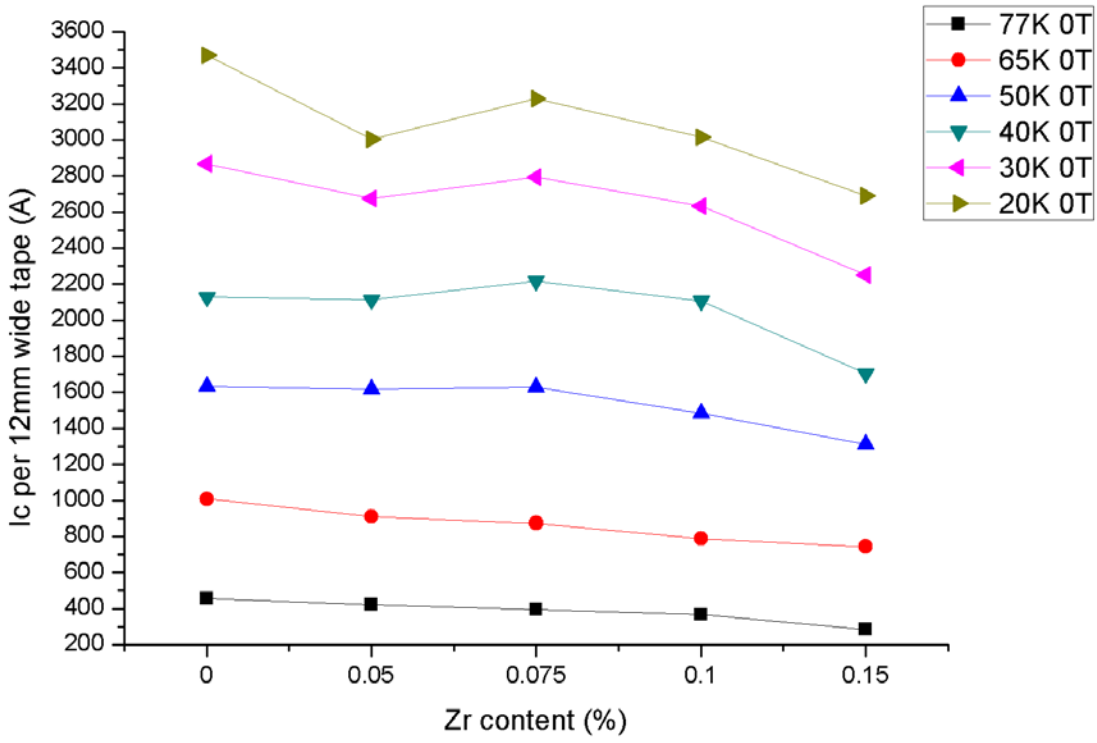

Fig. 3- 4 Temperature and Zr-doping content dependence of self-field J_c performance.

3.2 In-field performance of Zr-doped REBCO coated conductors

In order to systematically investigate the effect of Zr-doping on the in-field performance of REBCO coated conductors, a series of in-field measurements on REBCO coated conductor samples with different Zr contents up to 15% at temperatures between 20*K* to 77*K* with applied magnetic field up to 9*T* were performed. Discussion and data analysis with regard to these measurements are presented in this section.

3.2.1 Angular-dependent critical current performance

Fig. 3-5 shows the angular dependent critical currents at 77 *K* and 65 K with external field of 1T and 3T. The 0% Zr (undoped) sample showed a prominent *H*//*ab* peak in all the plots, while the samples with higher Zr-doping level showed wide *H*//*c* peaks that got flatter and wider as the field was increased from 1T to 3T. The high *H*//*ab* peak observed in the undoped REBCO sample is understandable considering the absence of BZO nanorods that hinder crystallinity along the *a*-*b* plane. Even though the *ab* peaks for Zr-doped samples were diminished drastically compared with that of the undoped sample, the presence of *c*-axis self-assembled BZO pinning centers in the films led to improved overall I_c values greatly. Also, the most significant I_c enhancement at 77*K* and 65*K* was achieved in samples with 5% and 7.5% Zr content levels. It can be seen that 15% Zr content sample showed much better I_c improvement at 65*K* than that at 77*K*, especially at a higher field.

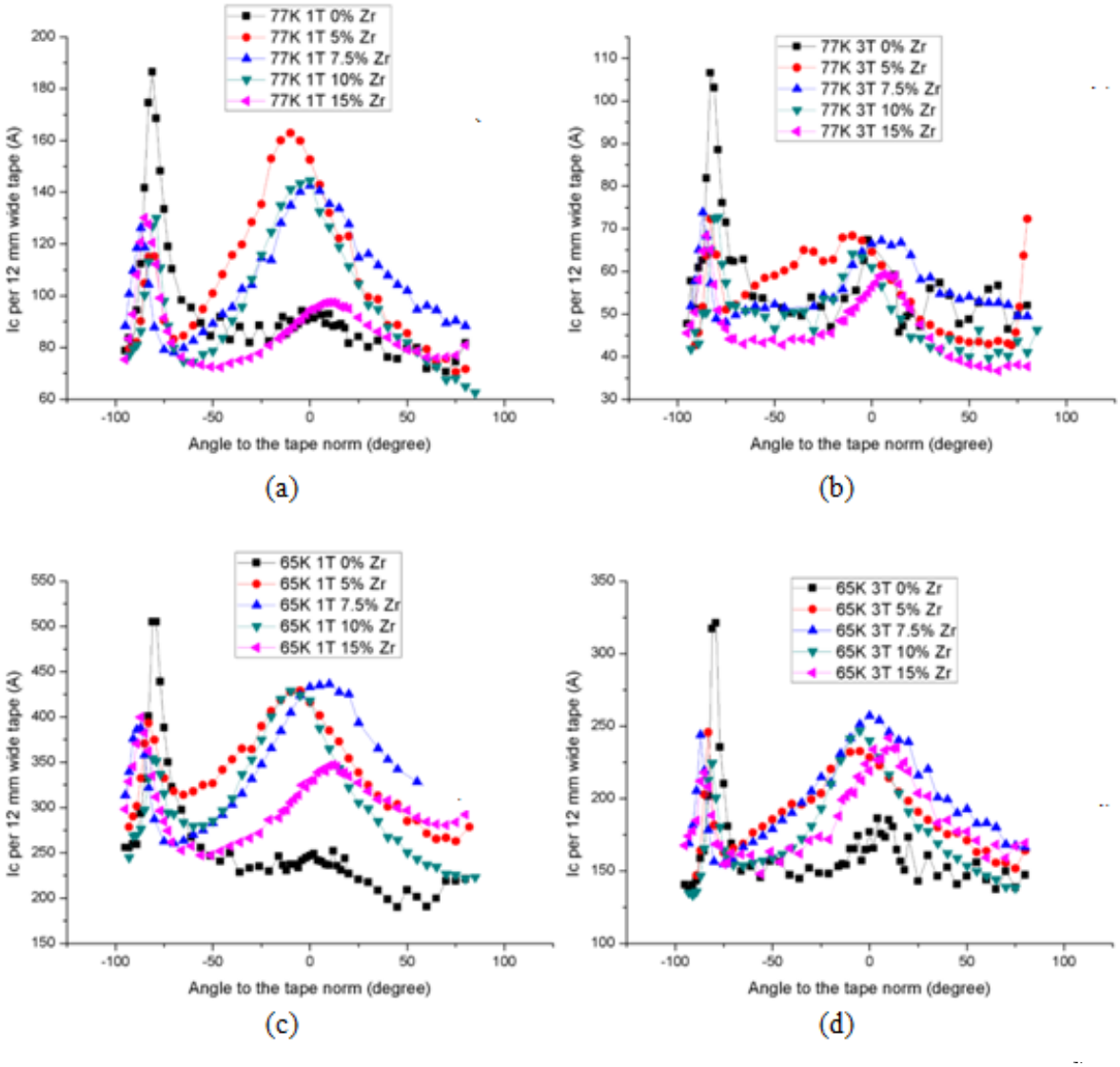

Fig. 3- 5 Temperature and Zr-doping content dependence of in-field performance at a) 77*K* and b) 65*K*.

Angular-dependent I_c at lower temperatures and higher fields are demonstrated in Fig. 3-6. As temperature became lower, the I_c of Zr-doped samples showed a dramatic increase whereas no such increase is seen in that of the undoped sample. An observation of interest is that as the magnetic field increased from 3 *T* to 7 *T* at a given temperature, the difference between undoped and doped samples with regard to I_c values at *H//c* was narrowed by a factor of three, while no significant differences are seen in the changes in the peaks at *H//ab*.

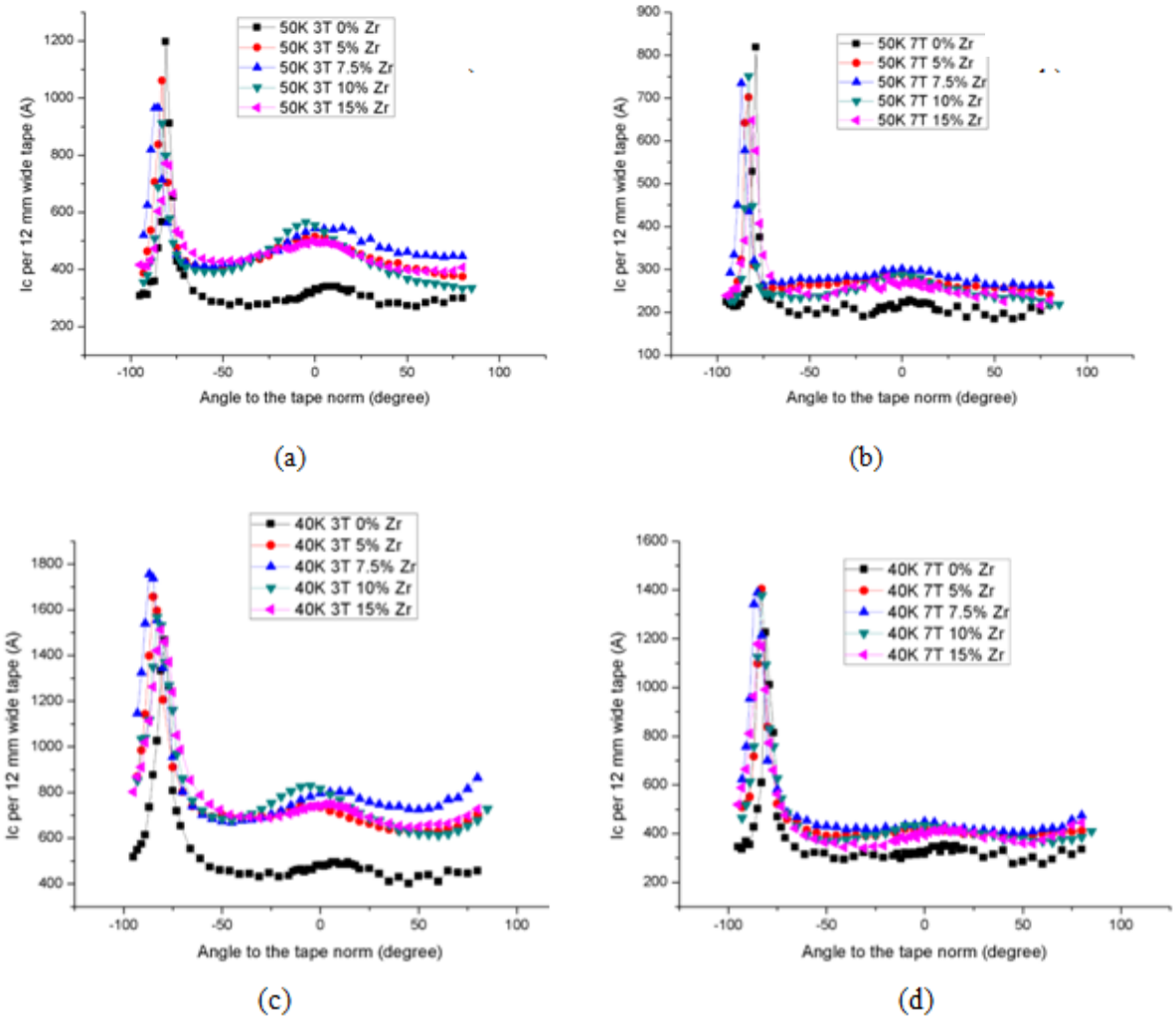

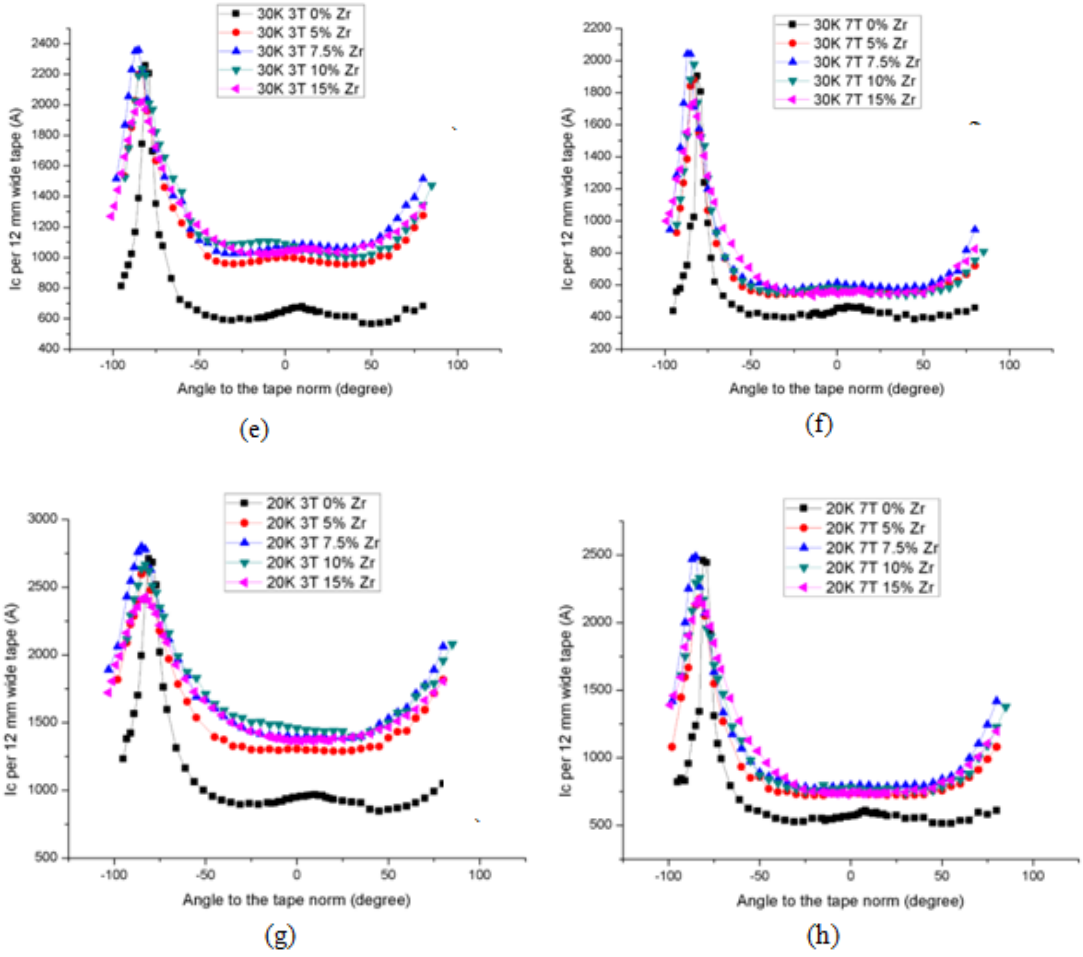

Fig. 3- 6 In-field angular dependence of critical current of Zr-doped REBCO samples at temperatures between 50*K* and 20*K*: (a) 50*K*, 3*T*; (b) 50*K*, 7*T*; (c) 40*K*, 3*T*; (d) 40*K*, 7*T*; (e) 30*K*, 3*T*; (f) 30*K*, 7*T*; (g) 20*K*, 3*T*; (h) 20*K* 7*T*.

The minimum critical current $I_{c,min}$ obtained during each angular-dependent I_c measurement was plotted in Fig. 3-7. The different behaviors of I_c values of undoped and doped samples can be interpreted by analyzing the Zr-doping effect on $I_{c,min}$, which is somewhat slight at 77K and even showed a decreasing trend in an external magnetic field of 3*T*. However, an increase of $I_{c,min}$ by a factor of two compared with that of the undoped sample was observed at lower temperatures and the optimum Zr-doping level for $I_{c,min}$ enhancement appeared after reaching 7.5% at 3T. Besides, samples with Zr-addition

content higher than 7.5% showed weaker enhancing effect on $I_{c,min}$ at 7T. Further analysis can be done by calculating the current retaining ratio R_r, as

$$R_r = \frac{I_{c,min}(T)}{I_{c,B=0}(T)}, \qquad (3\text{-}1)$$

where $I_{c,min}$ (T) is the minimum critical current obtained from the in-field angular-dependent I_c measurement at a certain temperature T, $I_{c,(B=0)}$ is the self-field critical current at T.

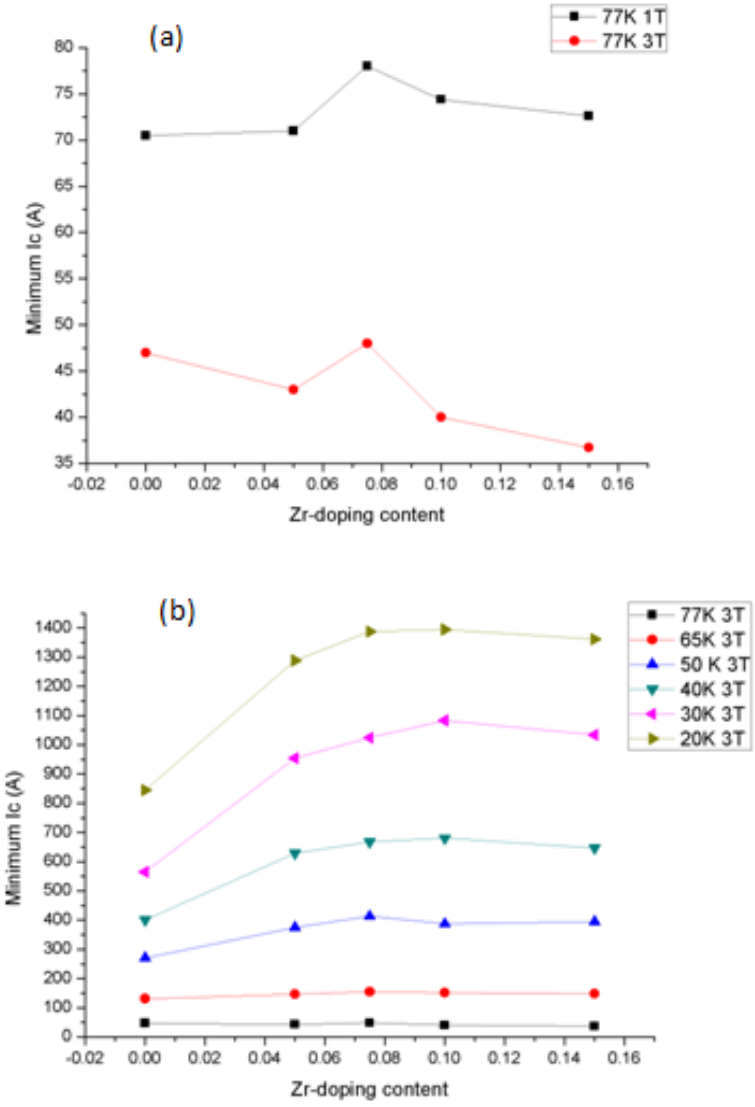

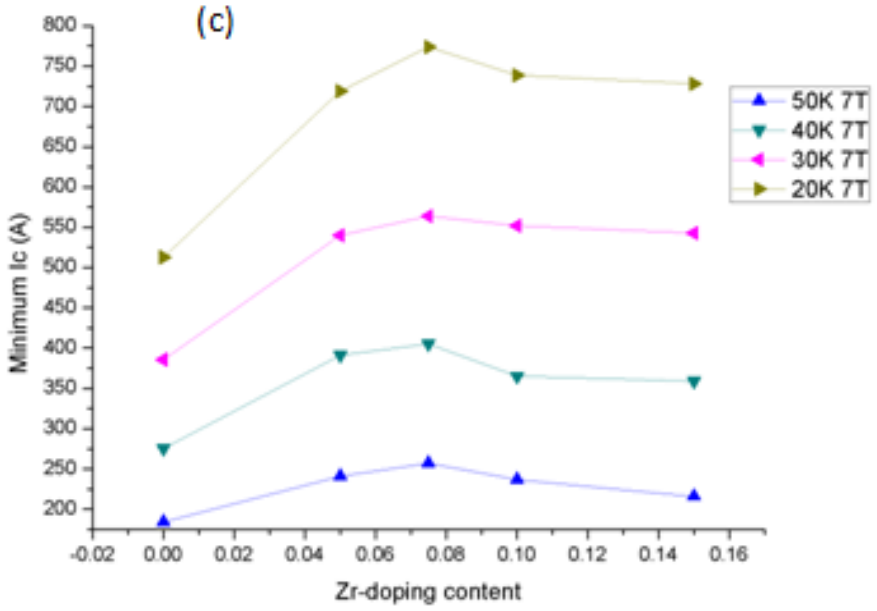

Fig. 3- 7 Temperature and field dependence of minimum critical currents in angular-dependent measurements of Zr-doped samples: (a) 77*K*; (b) 20*K* to 77*K* at 3*T*; (c) 20 to 50*K* at 7*T*.

The retained current ratio data is plotted in Fig. 3-8. It can be seen that the R_r value increased monotonously with increasing Zr doping level at all temperatures and fields. This trend confirmed that the presence of Zr dopant in REBCO thin film can enhance the minimum critical current and this enhancement is proportional to the Zr-doping content. It could be ascribed to the flux pinning effect by introducing BZO nanorods along c-axis and the randomly distributed rare-earth oxide nanoparticles in the REBCO thin films, which has been confirmed by PLD and MOD methods (A. Goyal 2007; Feldmann, Holesinger et al. 2010).

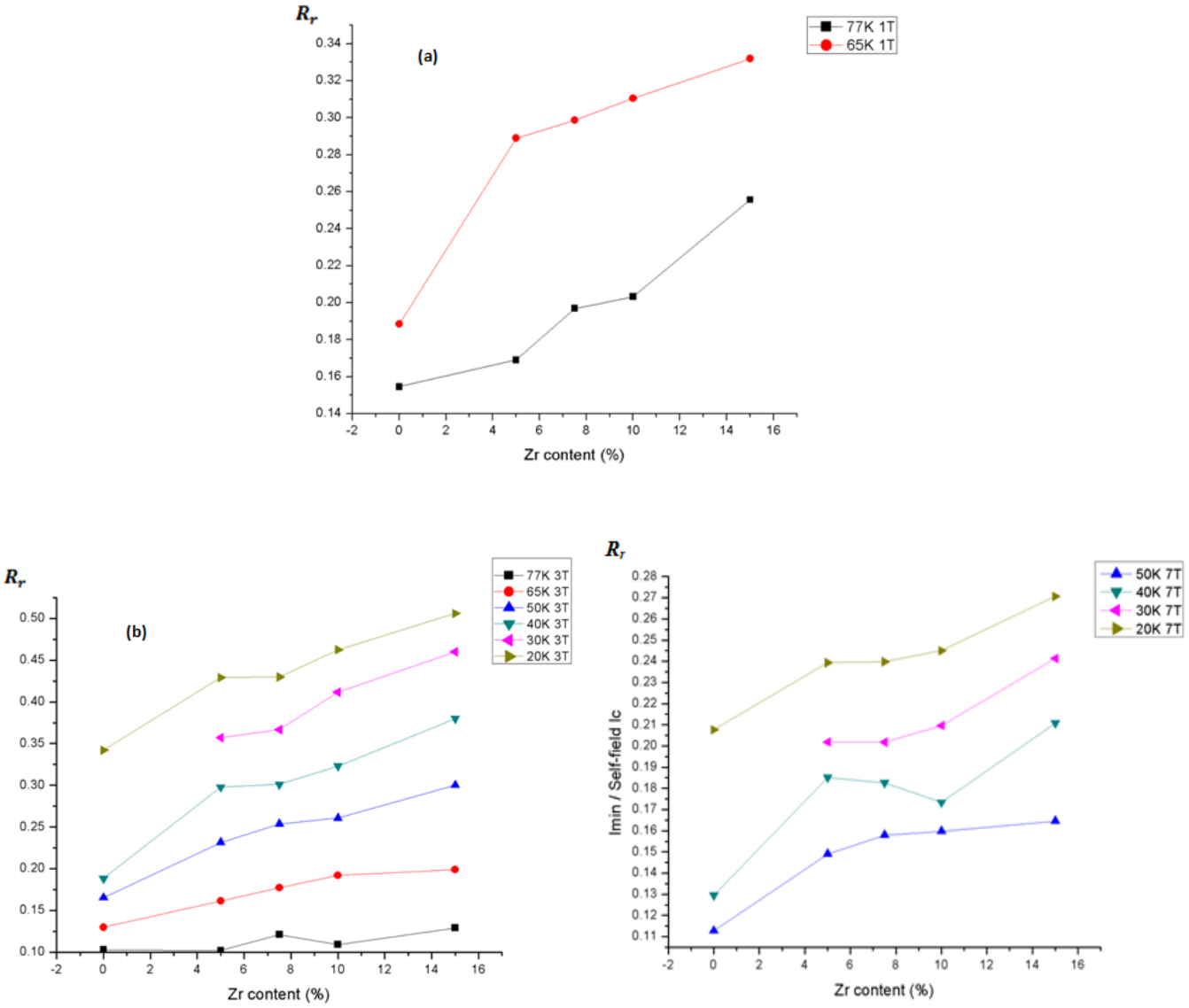

Fig. 3- 8 Temperature and field dependence of retained current ratio of Zr-doped samples: (a) 1*T*; (b) 3*T*; (c) 7*T*.

The dependence of the full-width-at-half-maximum (FWHM) of the J_c peak at *H//ab* with different Zr-doping levels is displayed in Fig. 3-9. It can be seen that the breadth of the J_c peak at *H//ab* increases with increasing Zr content at temperatures above 50K. This broadening is more pronounced at 30 K and 20 K. Specht et al. Specht et al. (Specht, Goyal et al. 2006) proposed that the annihilation of *a-b* plane stacking faults by rare-earth addition can result in the widening of J_c peak at *H//ab*. However, their work did not provide an explanation to the temperature dependence of the broadening of *H//ab* peaks with different Zr-doping levels. In the microstructural analysis section, more evidence on the pinning mechanism behind this broadening of Jc peak at *H//ab* is provided.

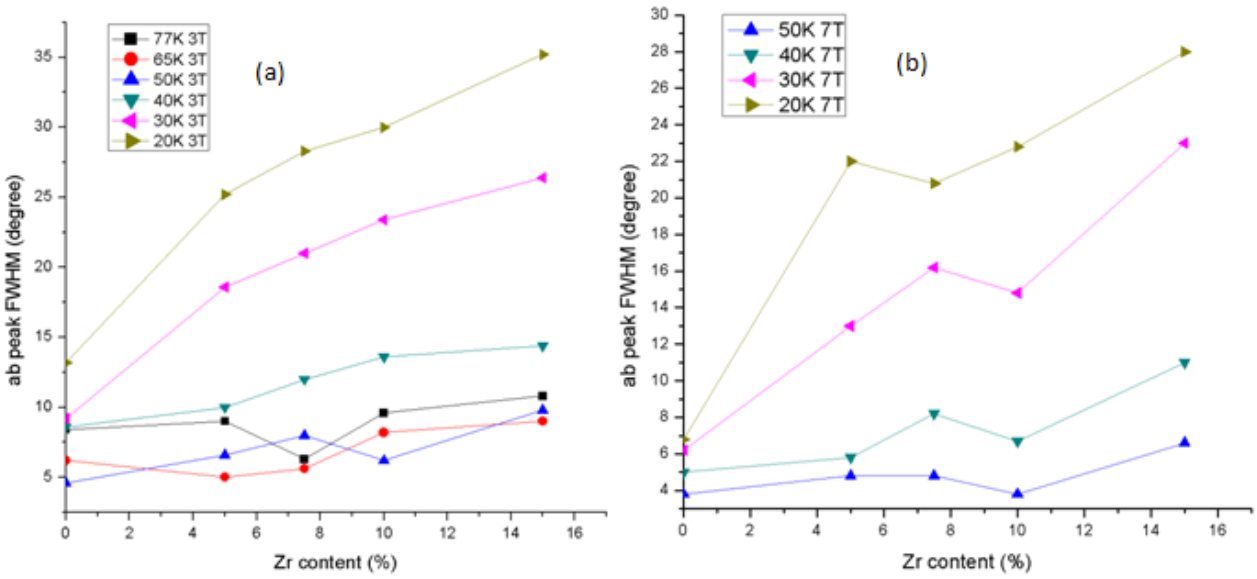

Fig. 3- 9 Zr-doping content and temperature dependence of the full-width-at- half-maximum of *H//ab* peak. The external field was 3*T* (a) and 7*T* (b) respectively.

3.2.2 Field-dependent critical current performance

After the angular-dependent measurements, the *H*//*ab* peak and *H*//*c* peak positions could be located to enable the subsequent field-dependent critical current measurements performed at these angle positions in external magnetic field up to 9T. The pinning force at these positions can be calculated as

$$F_p = J_c \times B, \tag{3-2}$$

where F_p is the pinning force, J_c is the critical current density, B is the magnetic field.

The *H*//*ab* field-dependent critical current and the pinning force data are both shown in Fig. 3-10. Plots with dash lines are for the field-dependent I_c data and those with solid lines are for the pinning force data. As can be seen in the data, the undoped sample showed obvious *H*//*ab* superiority over the Zr-doped samples in both the critical current and the pinning force values at all temperatures except 40 *K*. Here, the irregularity of the 40K data might be ascribed to bad measurements.

The improvement of the doped samples in the *H*//*ab* in-field performance became more and more prominent as the temperature dropped and the highest values were found to be at a Zr-doping content of 7.5%. Similar results were also reported in MOD-REBCO films doped with Zr (Zhou, Ghalsasi et al. 2007). The sample with 15% Zr content showed the lowest critical current value and pinning force compared to the rest of the samples including the undoped one.

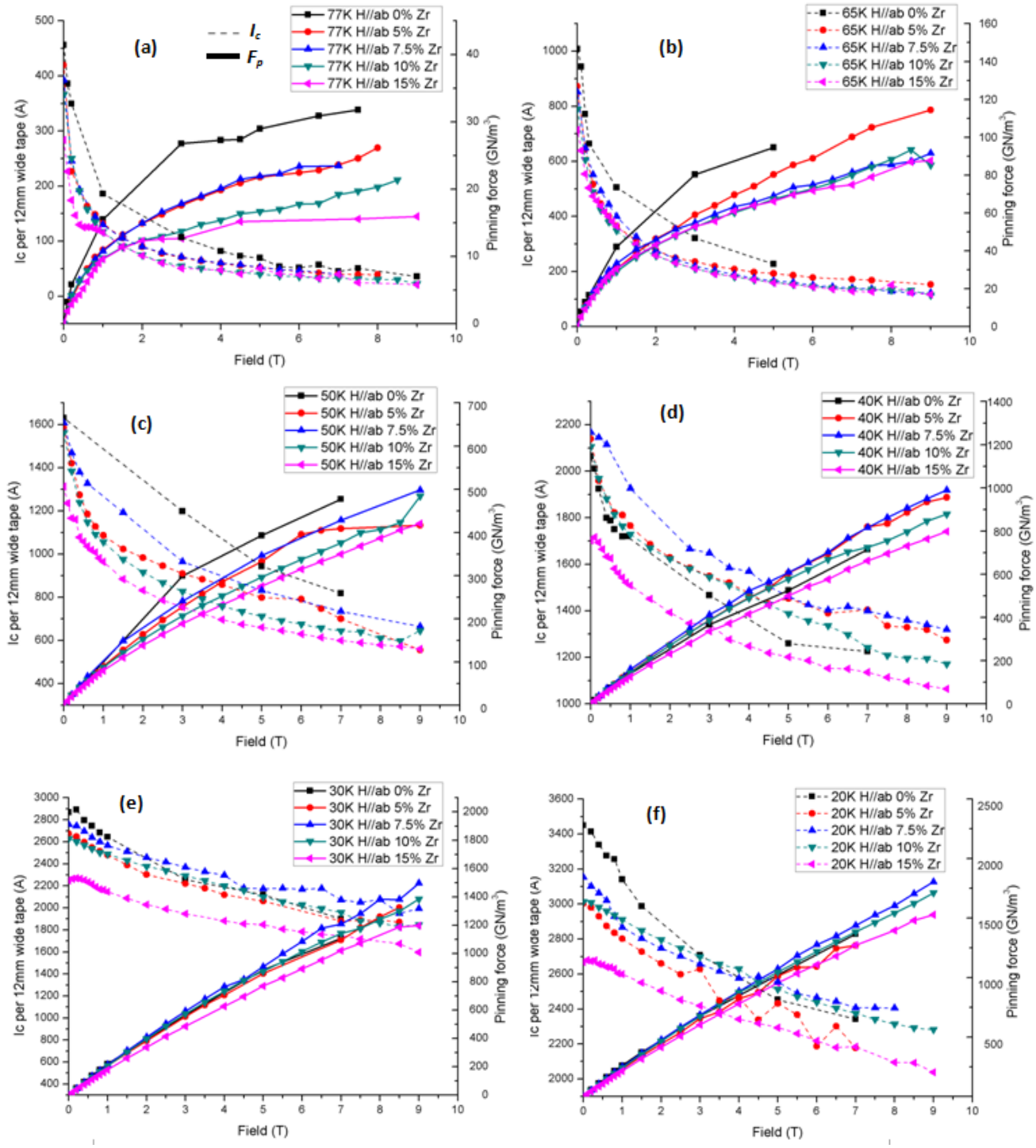

Fig. 3- 10 *H//ab* field-dependent critical current and pinning force dependence of Zr-doping content at various temperatures. a) 77*K*; b) 65*K*; c) 50*K*; d) 40*K*; e) 30*K*; f) 20*K*.

Dramatically different flux pinning behavior was observed in *H*//*c* critical current and the pinning force data shown in Fig. 3-11. The Zr-doped samples had much higher *H*//*c* I_c values compared to the undoped sample that could no longer demonstrate its excellence like it did in the *H* // *ab* peak critical current performance. The optimum Zr content was still 7.5%, while the sample with 15% Zr- doping level showed significant improvement and even exceeded the performance of the 7.5% sample at 65*K*. Another interesting fact was that the peak pinning forces shift to higher magnetic field as the temperature dropped. In other words, the field at which the highest pinning force of each sample increased as the temperature went lower. After the temperature decreased below 40*K*, no such maximum pinning force was detected up to 9*T*, which means that the pinning force would increase even beyond 9 T at such low temperatures.

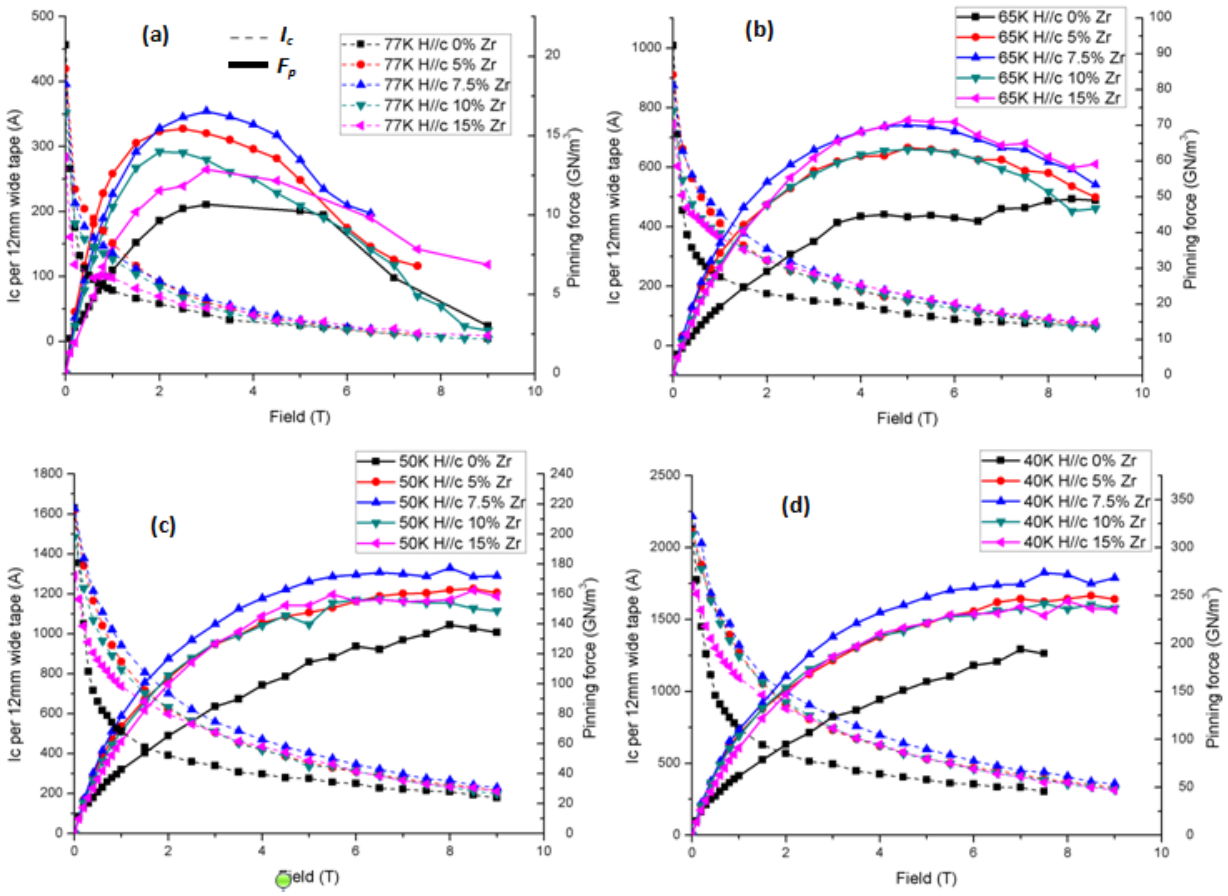

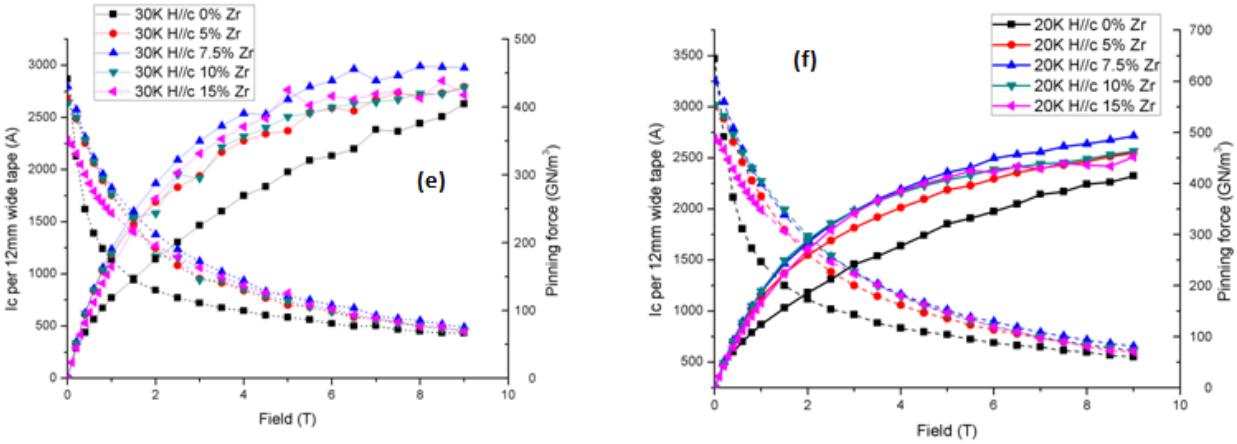

Fig. 3- 11 *H*//*c* field-dependent critical current and pinning force dependence of Zr-doping content at various temperatures. a) 77*K* ; b) 65*K*; c) 50*K*; d) 40*K*; e) 30*K*; f) 20*K*.

The strong *H*//*ab* peak in the undoped sample could be ascribed to the RE124 stacking fault intergrowth along the *ab* plane (W. Zhang 2007). Since the RE124 planar defect has a lattice parameter of 1.37 *nm*, it is very close to the effective pinning center size of REBCO, i.e., the short coherence length that is 1 to 2 *nm* (Zwerger 1997). As mentioned before, effective flux pinning can be achieved when the defects have comparable or slightly larger dimensions than the coherence length and distributed in a proper manner to match the density of vortices present in the superconductor. This is often referred as 'field matching' (Strickland, Long et al. 2008). Thus, the RE124 stacking fault could function as strong 2-D pinning centers to enhance the *H*//*ab* critical current. After Zr-doping into the REBCO thin films, the out-of-plane growth of BZO nanorods could inhibit the intergrowth of RE124 stacking faults and suppress the critical current at *H*//*ab*.

In order to explain the temperature and field dependence of the critical current data, the relationship between coherence length and effective pinning effect has to be

considered. On one hand, according to BCS and G-L theories, the coherence length ξ increases as the temperature decreases and approaches a constant value of ξ_0, the coherence length at 0 *K* (Lemberger, Ginsberg et al. 1978). The increased coherence length ξ with decreased temperature could become comparable to the dimensions of the RE_2O_3 nanoparticles and BZO nanorods and hence the pinning effects could become stronger at lower temperatures. The density of vortices penetrating a superconductor becomes higher as the magnetic field increases. Higher Zr-doping content could result in higher BZO nanorod density which is favorable for the flux pinning purpose at higher external field. In this way, the stronger flux pinning effect from Zr-doping at lower temperatures and higher field can be understood.

In this section, the in-field critical current performance of Zr-doped REBCO coated conductors was presented and discussed. Some trends of interest with regard to the temperature and field dependence of the critical current of samples with different Zr contents were observed:

1. The undoped sample showed prominent *H*//*ab* peaks at temperatures above 50 *K*, while its *H*//*c* peak values were much lower than those of Zr-doped samples at all temperatures.

2. The *H*//*ab* peaks of Zr-doped samples were diminished significantly compared with the undoped sample, but wide H//*c* peaks were seen above 65 *K* in these Zr-doped samples. The optimal Zr content exhibiting the best critical current performance was 7.5%.

3. The addition of Zr to the films could bring significant improvement in the minimum I_c and the optimal Zr content to obtain the highest minimum I_c was found to be 7.5%.

4. The retained current ratio and the FWHM of *H*//*ab* peaks increased monotonously with higher Zr-doping levels.

5. The undoped sample maintained its superiority of stronger *H*//*ab* pinning strength over that of the doped samples at all temperatures but 40K, while the doped samples showed much higher *H*//*c* critical current values and pinning forces.

6. The 15% Zr-doped sample showed the lowest *H*//*ab* critical current value and pinning force, while its *H*//*c* performance showed significant improvement.

7. The 7.5% Zr-doped sample showed the strongest pinning force across the temperature range.

Even though some explanations and discussions were provided, further evidence is still required to understand the flux pinning mechanism behind these phenomena. In the following section, more information about the relationship between the pinning effects and the microstructure are presented.

3.3 Microstructural study of Zr-doped REBCO superconductors

A general TEM cross-sectional image displaying the layered structure of the 15% Zr-doped REBCO coated conductor is shown in Fig. 3-12. More detailed microstructure

of Zr-doped REBCO thin film can be viewed in Fig. 3-13 where the planar and cross-sectional TEM images are displayed. Yellow solid lines are used to label the *c*-axis self-assembled BZO nanorods. An interesting phenomenon can be seen that no significant

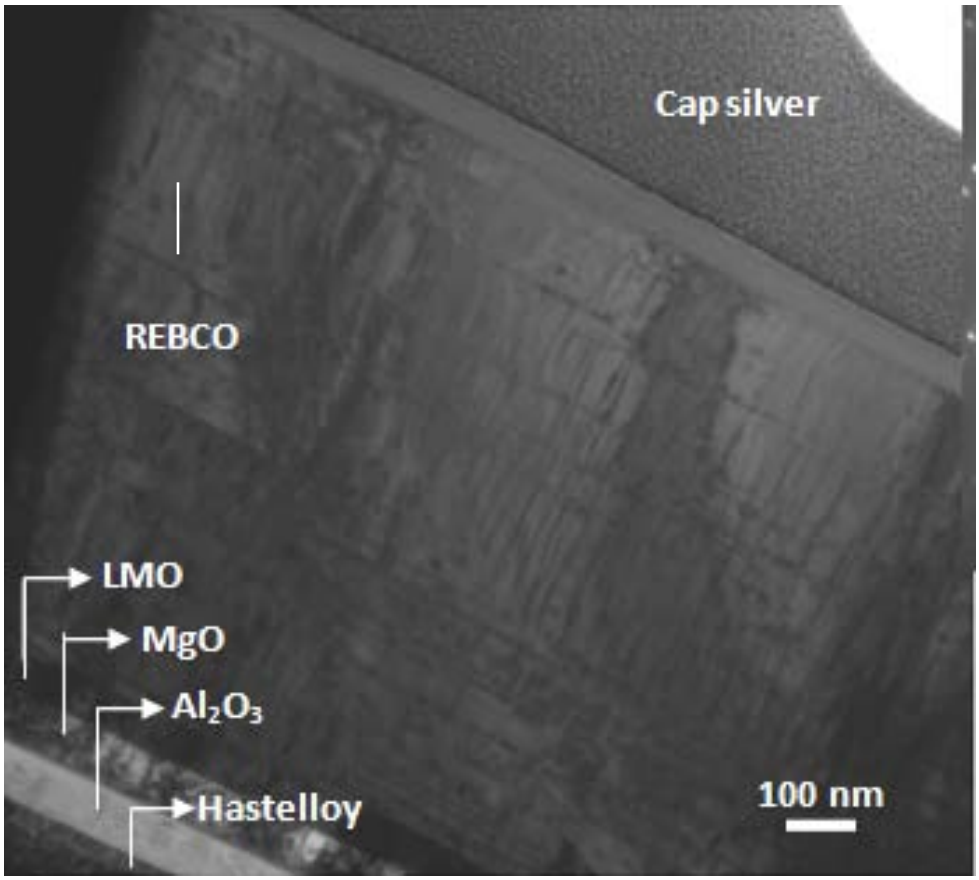

Fig. 3- 12 General cross-sectional view TEM photo of a Zr-doped REBCO coated conductor.

change in the size of these nanorods occurred as more Zr was added to the films, but the number density and the length of the nanorods showed dramatic increase. This trend might be useful to shed some light on the existence of optimum Zr content regarding to effective flux pinning as is discussed below.

It has been confirmed that the rise of impurity scattering rate in the material shortens the coherence length (Belova, Safonchik et al. 2011). The TEM images demonstrated that

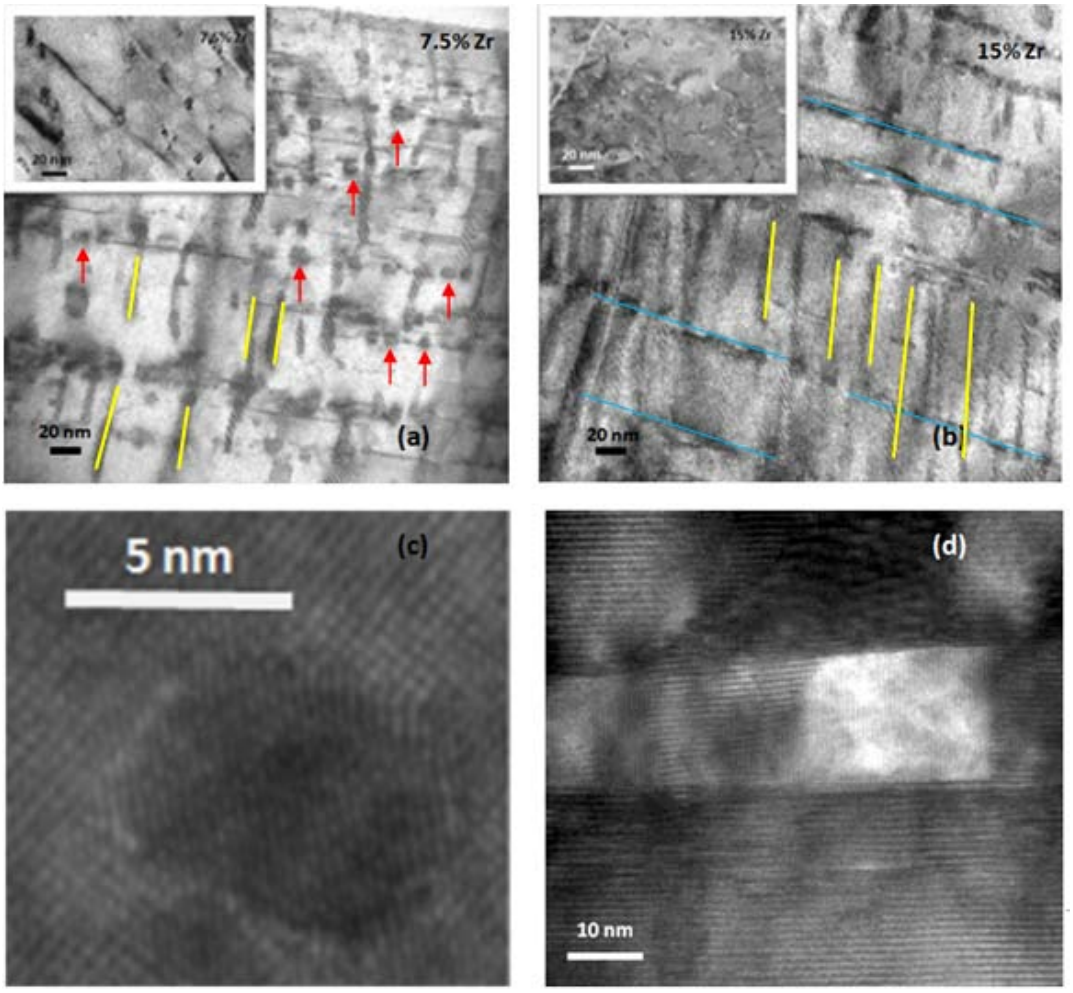

Fig. 3- 13 TEM planar (upper left) and cross-sectional views of the Zr-doped REBCO thin film with magnified photos of BZO nanorods and RE_2O_3 nanoparticles: a) 7.5% Zr-doped; b) 15% Zr-doped; c) BZO nanorod; d) RE_2O_3 nanoparticle.

higher Zr-doping level didn't result in an increase in the size, or the cross-sectional diameter of the BZO nanorods but an increase in the number density, which means the Zr scattering rate increased with the doping content. Thus, the addition of Zr to the film could reduce the coherence length. However, as was discussed in the previous section, lower temperatures could increase the coherence length and the pinning effectiveness of those large pinning centers. In this way, these two effects counteract with each other

when the Zr content and (or) the temperature change (s) and then an optimum Zr-content range can be determined for each temperature condition.

Since the precursor stoichiometry deviated far from that of the RE123 compound, the excess RE （Gd, Y） precursor resulted in the formation of RE_2O_3 nanoparticles, pointed by red arrows in Fig. 3-13, with sizes of 5-10 *nm* in the 7.5% Zr-doped sample, while planar RE_2O_3 defects, highlighed by blue solid lines, with dimensions between 10-20 nm were found in the 15% Zr-doped sample. The formation of RE_2O_3 precipitates in the films could affect the growth of BZO nanorods. Fig. 3-14 shows the 'blocking' effect from the planar growth of RE_2O_3. Some large particles and layers were found near the buffer layers in the sample with 15% Zr content, which is shown in Fig. 3-15. Similar secondary-phases were not seen in the 7.5% Zr-doped sample. The EDS results indicated that the former is CuO and the latter is RE_2O_3. The nucleation of these secondary-phases on top the buffer layers could affect the epitaxial growth of REBCO layers, and hence current percolation.

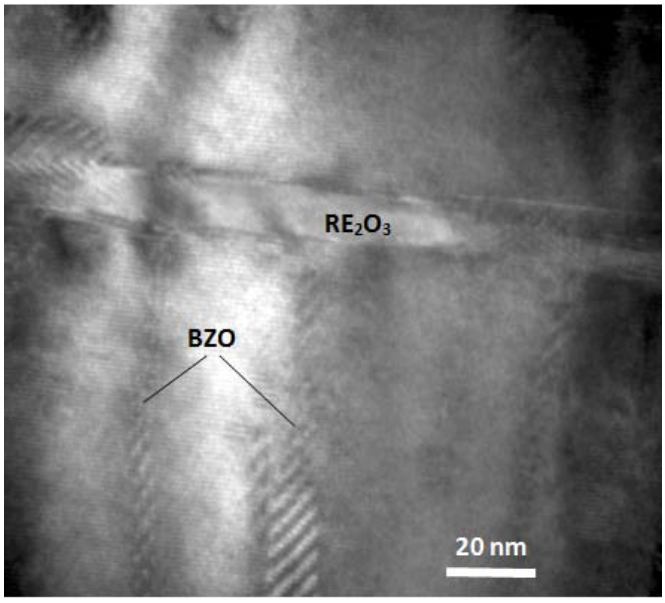

Fig. 3- 14 Planar RE_2O_3 layer blocking the growth of BZO nanorods by TEM.

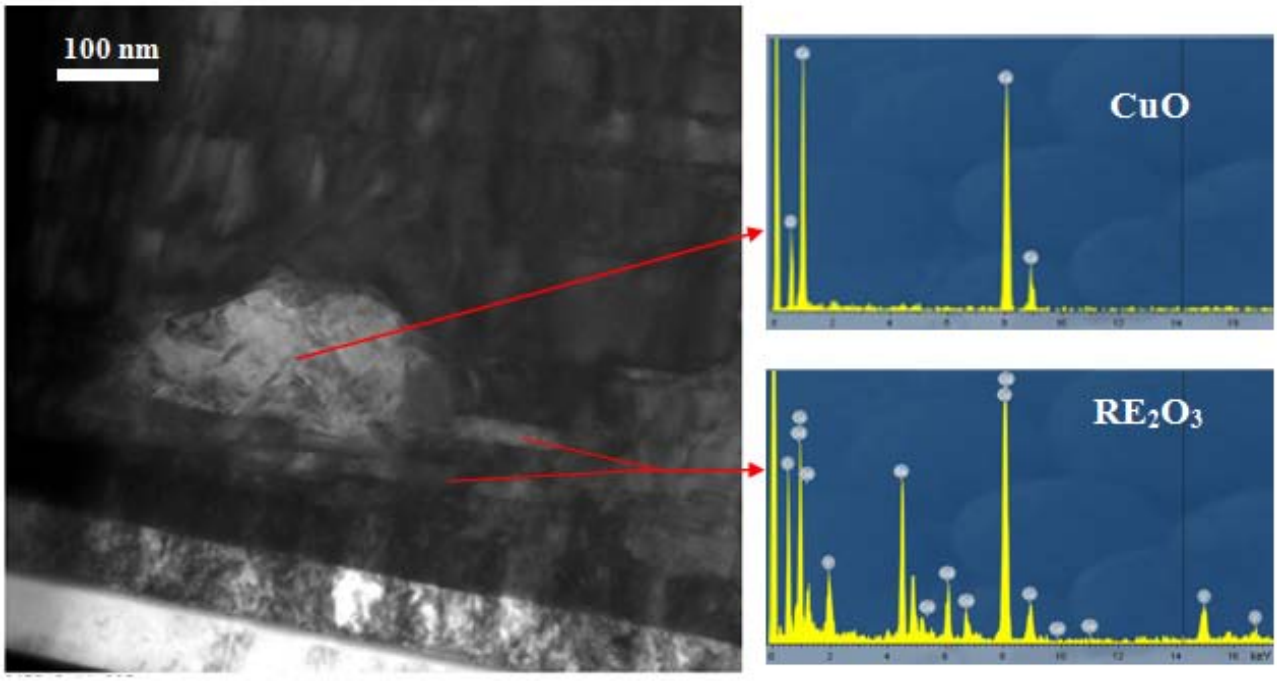

Fig. 3- 15 TEM image and EDS data of the secondary-phases near the buffer layers.

In this section, the microstructure of Zr-doped REBCO thin films was investigated using TEM and EDS techniques. The results indicated that:

1. The addition of Zr to the film could result in the coexistence of self-assembled BZO nanorods and RE_2O_3 precipitates as effective pinning centers.

2. Due to the temperature, magnetic field and chemical composition dependence of coherence length of REBCO, Zr-doping content would need to be optimized at different temperatures in order to achieve the best pinning effects.

3. The ramification of excessive Zr-doping to REBCO thin films is outgrowth of secondary-phases and (*001*) planar RE_2O_3 layers, which can affect both the epitaxial growth of REBCO layers and out-of-plane growth of BZO nanorods.

IV Summary and Conclusions

Due to the promise of various commercial applications, tremendous efforts have been put into the research of coated conductors for the last two decades. In order to realize the full potential of the HTS materials, intense research is being conducted to improve the in-field performance of these coated conductors.

Barium zirconium oxide (BZO) and rare-earth oxides (RE_2O_3) are found to be very effective pinning centers to enhance the pinning effects of REBCO thin films. Self-assembled BZO nanorods and RE_2O_3 precipitates can be fabricated simultaneously during the epitaxial growth of REBCO thin films using the MOCVD method to obtain synergistic pinning effects. The in-field properties at 77K of Zr-doped REBCO coated conductors have been studied in depth by many groups all over the world. However, no systematic work has been done on the low temperature and high magnetic field properties of Zr-doped REBCO coated conductors. The main goal of this thesis work was to fill in this gap and reveal more information on the relationship between the pinning effects and the temperature, field and chemical composition of Zr-doped REBCO coated conductors.

A wide temperature and magnetic field range was employed in the electromagnetic characterizations of REBCO coated conductor samples with 0%, 5%, 7.5%, 10% and 15% Zr content fabricated by the MOCVD method. All the critical current measurements were performed on a custom-made high field cryogen-free measurement system.

As the Zr content increased in the films, both the critical temperatures and self-field critical current values were found to decrease. XRD and ICP-MS data showed that as the Zr content in the precursor increased, more BZO phase was formed in the films.

The undoped REBCO sample showed a prominent *H*//*ab* peak in the angular-dependent critical current measurements and no significant *H*//*c* peak pinning over the entire temperature and field range studied. In contrast, samples doped with Zr exhibited diminished *H*//*ab* peaks and very strong *H*//*c* peaks especially at temperatures above 65*K* and fields up to 3*T*. Furthermore, the addition of Zr to the films dramatically improved the minimum critical current and the retained current ratio as the temperature was decreased and the field increased. In addition, higher Zr contents resulted in widened *H*//*ab* peaks during the angular-dependent critical current measurements. Zr-doped samples were superior to the undoped sample in both the overall critical current performance and the pinning force across the temperature and field range. And the Zr-doping content with the best pinning effects was found to be 7.5%.

C-axis oriented BZO nanorods with sizes of 5-10 *nm* were observed to coexist with RE_2O_3 precipitates with dimensions between 10 and 20 *nm* in the Zr-doped samples. No significant change in the size of these nanorods occurred as more Zr was added to the films, but the number density and the length of the nanorods showed dramatic increase. The high Zr-doping level also attributed to the nucleation of copper oxide particles and RE_2O_3 layers near the buffer layers which can affect the epitaxial growth of REBCO thin films.

The future work could be focused on the following aspects:

1) the superconducting properties of Zr-doped REBCO coated conductors at liquid helium temperature, i.e., 4.2 *K*;

2) searching for eligible effective pinning centers other than BZO nanorods to obtain more significant flux pinning effects;

3) systematic study of the influence from different rare-earth modifications to REBCO coated conductors;

4) solutions to the tape delamination problem.

References

A. D. Berry, D. K. G., R. T. Holm, E. J. Cukauskas, R. Kaplan, R. L. Henry (1988). "Formation of high Tc superconducting films by organometallic chemical vapor deposition." Applied Physics Letters **52**: 1743-1745.

A. Goyal, D. P. N., D. K. Christen, E. D. Specht, M. Paranthaman, D. M. Kroeger, J. D. Budai, Q. He, F. A. List, R. Feenstra, H. R. Kerchner, D. F. Lee, E. Hatfield (1996). "Epitaxial Superconductors on Rolling-assisted Biaxially-textured Substrates (RABiTS): A route Towards High Critical Current Density Wire." Applied Superconductivity **4**: 403-427.

A. Goyal, J. Li, P. M. Martin, A. Gapud, E. D. Specht, M. Paranthaman, X. Li, W. Zhang, T. Kodenkandath, and M. W. Rupich (2007). "Enhanced Flux-Pinning in Dy-Doped, MOD YBCO Films on RABiTS." IEEE Transaction on Applied Superconductivity **17**(2): 3340.

Arendt, P. N., Foltyn, S. R., Civale, L., DePaula, R. F., Dowden, P. C., Groves, J. R., Holesinger, T. G., Jia, Q. X., Kreiskott, S., Stan, L., Usov, I., Wang, H., Coulter, J. Y. (2004). "High critical current YBCO coated conductors based on IBAD MgO." Physica C: Superconductivity and its applications **412**(Journal Article): 795-800.

Ataru Ichinose, K. M., Masashi Mukaida, Yutaka Yoshida, Shigeru Horii, and Shirabe Akita (2005). "Microstructures of High-Tc Superconducting Films Having Artificial Pinning Centers." IEEE TRANSACTIONS ON APPLIED SUPERCONDUCTIVITY **15**.

Awaji, Satoshi, Namba, Masafumi, Watanabe, Kazuo, Miura, Masashi, Yoshizumi, Masateru, Izumi, Teruo, Shiohara, Yuh (2010). "Flux pinning properties of TFA-

MOD (Y,Gd)Ba2Cu3Oxtapes with BaZrO3nanoparticles." Superconductor Science and Technology **23**(1): 014006.

Satoshi Awaji, Masafumi Namba, Kazuo Watnabe, Shun Ito, Eiji Aoyagi, Hideki Kai, Masashi Mukaida, Ryusuke Kita (2009). "Flux pinning properties in BaMO[sub 3] (M=Zr,Sn) nanorod-introduced ErBa[sub 2]Cu[sub 3]O[sub x] films." Journal of Applied Physics **106**(10): 103915.

Aytug, T., Paranthaman, M., Specht, E. D., Zhang, Y., Kim, K., Zuev, Y. L., Cantoni, C., Goyal, A., Christen, D. K., Maroni, V. A., Chen, Y., Selvamanickam, V. (2010). "Enhanced flux pinning in MOCVD-YBCO films through Zr additions: systematic feasibility studies." Superconductor Science and Technology **23**(1): 014005.

B. Matthias, T. G., S. Geller, E. Corenzwit (1954). "Superconductivity of Nb3Sn." Physic. Rev.: 1435.

B.C. Richards, S.L. Cook, D.L. Pinch, G.W. Andrews, G. Lengeling, B. Schulte, H. Jürgensen, Y.Q. Shen, P. Vase, T. Freltoft, C.I.M.A. Spee, J.L. Linden, M.L. Hitchman, S.H. Shamlian, A. Brown (1995). "MOCVD of high quality YBa2Cu3O7−δ thin films using a fluorinated barium precursor." J. Phys. **IV(5)**: C5-407.

Bednorz, J. G. and K. A. Muller (1986). "Possible High-Tc Superconductivity in the Ba-La-Cu-O System." Zeitschrift Fur Physik B-Condensed Matter **64**(2): 189-193.

Belova, P., Safonchik, M., Traito, K. B., Lähderanta, E. (2011). "Coherence length of magnetic field in the mixed state of type-II superconductors." Journal of Physics: Conference Series **303**: 012114.

Benazzouz, F., Zouaoui, M., Mellekh, A., Annabi, M., Vantendeloo, G., Bensalem, M. (2007). "Flux pinning by Al-based nanoparticles embedded in YBCO: A transmission electron microscopic study." Physica C: Superconductivity **455**(1-2): 19-24.

Braccini, V., Xu, A., Jaroszynski, J., Xin, Y., Larbalestier, D. C., Chen, Y., Carota, G., Dackow, J., Kesgin, I., Yao, Y., Guevara, A., Shi, T., Selvamanickam, V. (2011). "Properties of recent IBAD–MOCVD coated conductors relevant to their high field, low temperature magnet use." Superconductor Science and Technology **24**(3): 035001.

Chen-Fong Tsai, Y. Z., Li Chen, and Haiyan Wang (2011). "Flux Pinning Properties in YBCO Thin Films With Self-Aligned Magnetic Nanoparticles." IEEE Transaction on Applied Superconductivity **21**: 2749.

Chen, Yimin, Selvamanickam, Venkat, Zhang, Yifei, Zuev, Yuri, Cantoni, Claudia, Specht, Eliot, Paranthaman, M. Parans, Aytug, Tolga, Goyal, Amit, Lee, Dominic (2009). "Enhanced flux pinning by BaZrO[sub 3] and (Gd,Y)[sub 2]O[sub 3] nanostructures in metal organic chemical vapor deposited GdYBCO high temperature superconductor tapes." Applied Physics Letters **94**(6): 062513.

D. M. Frigo, G. J. M. v. E., P. J. Reuvers, C. J. Smit (1994). "Preparation and properties of alane dimethylethylamine, a liquid precursor for MOCVD." Chem. Mater. **6**: 190-195.

D.H. Kim, K. E. G., R.T. Kampwirth and J.C. Smith (1991). "Effect of Cu-O layer spacing on the magnetic field induced resistive broadening of high-temperature superconductors." Physica C **177**: 431-437.

M. Damling, J. M. Seuntjens, D. C. Larbalestier (1990). "Oxygen-defect flux pinning , anomalous magnetization and intra-grain granularity in YBa2Cu3O7-x." Nature(346).

Dew-Hughes, D. (2001). "The critical current of superconductors: an historical review." Low Temperature Physics **27**(9): 713.

Díaz, A., Mechin, L., Berghuis, P., Evetts, J. E. (1998). "Evidence for Vortex Pinning by Dislocations in YBa_{2}Cu_{3}O_{7-δ} Low-Angle Grain Boundaries." Physical Review Letters **80**(17): 3855-3858.

Dimos, D., Chaudhari, P., Mannhart, J. (1990). "Superconducting transport properties of grain boundaries in YBa2Cu3O7 bicrystals." Physical Review B **41**(7): 4038-4049.

Ekin, J. W., Salama, K., Selvamanickam, V. (1991). "High-transport current density up to 30 T in bulk YBa2Cu3O7 and the critical angle effect." Applied Physics Letters **59**(3): 360.

Emergo, R. L. S. (2009). Enhancing Jc(B,θ) in YBa2Cu3O7-δ via nano-engineering of pinning structures, University of Kansas.

F. London, H. L. (1935). "The Electromagnetic Equations of the Supraconductor." Proc. Roy. Soc.: 71.

Ding Fa-Zhu, Gu Hong-Wei, Zhang Teng, Dai Shao-Tao, Xiao Li-Ye (2011). "Influence of oxygen pressure on critical current density and magnetic flux pinning structures in YBa 2 Cu 3 O 7− x fabricated by chemical solution deposition." Chinese Physics B **20**(2): 027402.

Fazhu Ding, H. G., Teng Zhang, Hongyan Wang, Fei Qu, Shaotao Dai,Xingyu Peng, Jiangli Cao (2012). "Enhanced flux pinning in MOD-YBCO films with co-doping of BaZrO3 and Y2O3 nanoparticles." Journal of Alloys and Compounds(513): 277-281.

Feldmann, D. M., Holesinger, T. G., Maiorov, B., Foltyn, S. R., Coulter, J. Y.,Apodaca, I. (2010). "Improved flux pinning in YBa2Cu3O7with nanorods of the double perovskite Ba2YNbO6." Superconductor Science and Technology **23**(9): 095004.

Gao, L., Huang, Z. J., Meng, R. L., Lin, J. G., Chen, F., Beauvais, L., Sun, Y. Y., Xue, Y. Y., Chu, C. W. (1993). "Study of Superconductivity in the Hg-Ba-Ca-Cu-O System." Physica C-Superconductivity and Its Applications **213**(3-4): 261-265.

Godeke, A., Denouden, A., Nijhuis, A., Tenkate, H. (2008). "State of the art powder-in-tube niobium–tin superconductors." Cryogenics **48**(7-8): 308-316.

Haruta, M., Fujiyoshi, T., Sueyoshi, T.,Dezaki, K., Ichigosaki, D.,Miyahara, K., Miyagawa, R., Mukaida, M., Matsumoto, K., Yoshida, Y., Ichinose, A., Horii, S. (2006). "Flux pinning properties of ErBa2Cu3Oy thin films with BaZrO3 nanorods." Superconductor Science and Technology **19**(8): 803-807.

Hawsey, R. and D. Christen (2006). "Progress in research, development, and pre-commercial deployment of second generation HTS wires in the USA." Physica C: Superconductivity **445-448**: 488-495.

Holesinger, T. G, Civale, L., Maiorov, B., Feldmann, D. M, Coulter, J. Y, Miller, D. J, Maroni, V. A, Chen, Z., Larbalestier, D. C, Feenstra, R., Li, X., Huang, Y., Kodenkandath, T., Zhang, W., Rupich, M. W, Malozemoff, A. P (2008).

"Progress in Nanoengineered Microstructures for Tunable High-Current, High-Temperature Superconducting Wires." Advanced Materials **20**(3): 391-407.

Housecroft, C. E. and A. G. Sharpe, Eds. (2004). Inorganic Chemistry, Prentice Hall.

Inada, R., Iwata, Y., Tateyama, K., Nakamura, Y., Oota, A., Zhang, P. X. (2006). "AC losses in Ag-sheathed Bi2223 tapes with Ca2CuO3 as interfilamentary resistive barriers." Physica C: Superconductivity **445-448**: 762-767.

J. Bardeen, L. C., J. R. Schrieffer (1957). "Microscopic Theory of Superconductivity." Phys. Rev. **106**: 162-164.

J. G. Noudem, E. S. R., M. Tarka, M. Noe and G. J. Schmitz (2001). "Melt-texture joining of YBa2Cu3Oy bulks." Supercond. Sci. Technol. **14**: 363.

J. G. Wen, S. M., W. Ito, T. Morishita, and N. Koshizuka (1994). "Direct high-resolution electron microscopy observations of sputtered a-axis oriented YBa2Cu3O7 films prepared by a self-template method on SrTiO3 substrates " Appl. Phys. Lett. **64**: 3334.

J. R. Groves, P. N. A., S. R. Foltyn, Q. X. Jia, T. G. Holesinger, L. A. Emmert, R. F. DePaula, P. C. Dowden, and a. L. Stan (2003). "Improvement of IBAD MgO Template Layers on Metallic Substrates for YBCO HTS Deposition." IEEE Transaction on Applied Superconductivity **13**.

J. W. Ekin, A. I. B., A. J. Panson, M. A. Janocko, D. W. Capone, N. J. Zaluzec, B. Flandermeyer, O. F. de Lima, M. Hong, J. Kwo, and S. H. Liou (1987). "Evidence for weak link and anisotropy limitations on the transport critical current in bulk polycrystalline Y1Ba2Cu3Ox." Appl. Phys. **62**(4821).

Jin, S., Tiefel, T. H., Sherwood, R. C., Davis, M. E., van Dover, R. B., Kammlott, G. W., Fastnacht, R. A., Keith, H. D. (1988). "High critical currents in Y-Ba-Cu-O superconductors." Applied Physics Letters **52**(24): 2074.

K. Kimura, M. S., K. Miyamoto, H. Hashimoto, K. Watanabe, S. Awaji, N. Kobayashi (1995). Advances in Superconductivity VII: 851.

Kramer, M. J. (1991). "Processing controlled stacking faults in YBa2Cu3O7-x and their effect on flux pinning." Appl. Phys. Lett. **58**(10): 1086.

Lemberger, Thomas, Ginsberg, D., Rickayzen, G. (1978). "Calculation of the electromagnetic coherence length in superconductors with magnetic impurities." Physical Review B **18**(11): 6057-6065.

Lihua Chen, H. C., A P Paulikas, Hong Zheng and B W Veal (2002). "Joining of melt-textured YBCO: a direct contact method." Supercond. Sci. Technol.(15): 672-674.

M.W. Rupich, W. Z., X . Li, T. Kodenkandath, D.T. Verebelyi, U. Schoop, C. Thieme, M. Teplitsky, J. Lynch, N. Nguyen, E. Siegal, J. Scudiere, V. Maroni, K. Venkataraman, D. Miller, T.G. Holesinger (2004). "Progress on MOD/RABiTSTM 2G HTS wire." Physica C: Superconductivity **412-414**: 877-884.

Mele, P., Matsumoto, K., Horide, T., Ichinose, A., Mukaida, M., Yoshida, Y., Horii, S., Kita, R. (2008). "Incorporation of double artificial pinning centers in YBa2Cu3O7−δ films." Physica C: Superconductivity **468**(15–20): 1631-1634.

Nick M. Strickland, E. F. T., James A. Xia, Nicholas J. Long (2009). "Flux Pinning by Barium Stannate Nanoparticles in MOD YBCO Coated Conductors." IEEE Transaction on Applied Superconductivity **19**(3): 3140.

Onnes, H. K. (1911). Leiden Commun.: 124C.

P, D. M. (2000). Physica C **329**: 257.

Q. Zhong, P.C. Chou, Q.L. Li, G.S. Taraldsen, A. Ignatiev (1995). "High-rate growth of purely a-axis oriented YBCO high-Tc thin films by photo-assisted MOCVD." Physica C **246**.

Robin A. Gardiner, D. C. G., Gregory T. Stauf, Brian A. Vaartstra, Robert L. Ostrander, Arnold L. Rheingold (1994). "Mononuclear Barium Diketonate Polyamine Adducts. Synthesis, Structures, and Use in MOCVD of Barium Titanate." Chem. Mater. **6**: 1967-1970.

Rupich, M. W., Li, X., Sathyamurthy, S., Thieme, C., Fleshler, S. (2011). "Advanced development of TFA-MOD coated conductors." Physica C: Superconductivity **471**(21-22): 919-923.

Salama, K., Selvamanickam, V., Gao, L., Sun, K. (1989). "High current density in bulk YBa2Cu3Ox superconductor." Applied Physics Letters **54**(23): 2352.

Saxena, A. K., Ed. (2010). HIgh-temperature superconductors. Heidelberg, Springer.

Schlachter, S., Frank, A., Ringsdorf, B., Orschulko, H., Obst, B., Liu, B., Goldacker, W. (2006). "Suitability of sheath materials for MgB2 powder-in-tube superconductors." Physica C: Superconductivity **445-448**: 777-783.

Schneemeyer, L. F., Gyorgy, E. M., Waszczak, J. V. (1987). "Magnetic characterization of rare-earth barium cuprate superconductors." Phys Rev B Condens Matter **36**(16): 8804-8806.

V. Selvamanickam, M. Mironova, S. Son, K. Salama (1993). "Flux pinning by dislocations in deformed melt-textured YBa2Cu3Ox superconductors." Physica C **208**: 238-244.

Shi, T. (2011). STUDY OF STRUCTURE AND ELECTROMAGNETIC PROPERTIES OF ZIRCONIUM-DOPED REBA2CU3O7-X SUPERCONDUCTING FILMS FABRICATED BY METAL ORGANIC CHEMICAL VAPOR DEPOSITION, University of Houston. **Master's:** 96.

Shuu'ichirou Yamamoto, A. K., Kouji Nagata, Takeo Hattori, and S. Oda (1997). "Atomic layer-by-layer epitaxy of oxide superconductors by MOCVD." Applied Surface Science **112**: 30-37.

Specht, E. D., Goyal, A., Li, J., Martin, P. M., Li, X., Rupich, M. W. (2006). "Stacking faults in YBa[sub 2]Cu[sub 3]O[sub 7−x]: Measurement using x-ray diffraction and effects on critical current." Applied Physics Letters **89**(16): 162510.

Strickland, N. M., Long, N. J., Talantsev, E. F., Hoefakker, P., Xia, J., Rupich, M. W., Kodenkandath, T., Zhang, W., Li, X., Huang, Y. (2008). "Enhanced flux pinning by BaZrO3 nanoparticles in metal-organic deposited YBCO second-generation HTS wire." Physica C: Superconductivity **468**(3): 183-189.

Sytnikov, V. E., Vysotsky, V. S., Radchenko, I. P., Polyakova, N. V. (2008). "1G versus 2G-comparison from the practical standpoint for HTS power cables use." Journal of Physics: Conference Series **97**: 012058.

T Habisreuther, D. L., T Strasser, M Wu (1998). "Using Melt-textured YBCO for Sperconducting Electromotors." Supercondcutors Overview: 31.

T.A. Prikhna, W. G., V.E. Moshchil, L.S. Uspenskaya, R. Viznichenko, N.V. Sergienko, A. Kordyuk, V. Sverdun, and D. L. A. Surzhenko, T. Habisreuther, A. Vlasenko (2003). "Superconducting joining of MT-YBCO." Physica C: Superconductivity **392-396**: 432-436.

Tachiki, M. and S. Takahashi (1989). "Strong Vortex Pinning intrinsic in High-Tc Oxide Superconductors." Solid State Communication **70**: 291-295.

Takafumi Kimura, H. Y., Hideaki Machida, Hiroshi Kokubun and Masao Yamada (1994). "Synthesis of Novel Sr Sources for Metalorganic Chemical Vapor Deposition of SrTiO3." J. Appl. Phys. **33**: 5119.

Tang, Chenyi, Yao, Xin, Hu, Jian, Rao, Qunli, Li, Yanrong, Tao, Bowan, "YBCO melt-textured growth seeded by superheating YBCO/MgO thin film." Superconductor Science and Technology **18**(6): L31-L34.

Troger, L. (1992). J. Apl. Phys. **72**.

Ueyama, M. and K. Ohkura (1996). "Development of Ag-sheathed Bi(2223) superconducting wires and coils." Physica C **263**: 172-175.

V. Ginzburg, L. L. (1950). Zh. Eksp. Teor. Fiz.: 1064.

W. Ito, S. M., S. Okayama, Y. Yoshida and T. Morishita (1994). "Optical emission spectroscopic studies on the growth of YBCO thin films by dc-94.92 MHz hybrid plasma sputtering." J. Mater. Res **9**.

W. Meissner, R. O. (1933). "Ein neuer Effekt bei Eintritt der Supraleitfähigkeit." Naturwissenschaften **21**(44): 787-788.

Zhang, W., Rupich, M. W., Schoop, U., Verebelyi, D. T., Thieme, C. L. H., Li, X.,Kodenkandath, T., Huang, Y., Siegal, E., Buczek, D., Carter, W.,

Nguyen, N., Schreiber, J., Prasova, M., Lynch, J., Tucker, D.,Fleshler, S. (2007). "Control of flux pinning in MOD YBCO coated conductors." IEEE Transaction on Applied Superconductivity **17**(2): 3347.

Wang, C. P., Do, K. B., Beasley, M. R., Geballe, T. H., Hammond, R. H. (1997). "Deposition of in-plane textured MgO on amorphous Si[sub 3]N[sub 4] substrates by ion-beam-assisted deposition and comparisons with ion-beam-assisted deposited yttria-stabilized-zirconia." Applied Physics Letters **71**(20): 2955.

Wang, J., Kwon, J. H., Yoon, J., Wang, H., Haugan, T. J., Baca, F. J., Pierce, N. A.,Barnes, P. N. (2008). "Flux pinning in YBa[sub 2]Cu[sub 3]O[sub 7−δ] thin film samples linked to stacking fault density." Applied Physics Letters **92**(8): 082507.

Wu, M. K., Ashburn, J. R., Torng, C. J., Hor, P. H., Meng, R. L., Gao, L., Huang, Z. J.,Wang, Y. Q., Chu, C. W. (1987). "Superconductivity at 93-K in a New Mixed-Phase Y-Ba-Cu-O Compound System at Ambient Pressure." Physical Review Letters **58**(9): 908-910.

X. D. Wu, S. R. F., P. Arendt, J. Townsend, C. Adams, I. H. Campbell, P. Tiwari, Y. Coulter, and D. E. Peterson (1994). "High current YBa2Cu3O7−δ thick films on flexible nickel substrates with textured buffer layers " Appl. Phys. Lett.(65): 1961.

Xuming Xiong, K. P. L., Jodi L. Reeves, Andrei Rar, Yunfei Qiao, Robert M. Schmidt, Yimin Chen, and Y.-Y. X. Yijie Li, and Venkat Selvamanickam (2007). "High Throughput Processing of Long-Length IBAD MgO and Epi-Buffer Templates at SuperPower." IEEE Transaction on Applied Superconductivity **17**(2): 3375.

Y. Feng, A. K. P., Y. Zhao, Y. Wu, N. Koshizuka and L. Zhou (2001). "Improved flux pinning in YxHo1-xBa2Cu3Oy fabricated by powder melting process." Superconductor Science and Technology **14**: 224-228.

Yasuhiro Iijima, N. T., Yoshimitsu Ikeno and Osamu Kohno (1991). "Biaxially Alligned Yba2Cu3O7-x thin film tapes." Physica C: 185-189.

Yimin Chen, T. S., Albert P. Guevara, Yangxin Zhang, Yao Yao, Ibrahim Kesgin, and Venkat Selvamanickam (2011). "Composition Effects on the Critical Current of MOCVD-Processed Zr:GdYBCO Coated Conductors in an Applied Magnetic Field." IEEE Transaction on Applied Superconductivity **21**(3): 3166.

Zama Hideaki, S. J., Hattori Takeo, Oda Shunri (1994). "Superconducting properties of ultrathin films of YBa2Cu3Ox prepared by metalorganic chemical vapor deposition at 500°C." Japanese Journal of Applied Physics **3A**: 33.

Zhang Pingxiang, Z. L., Ji Ping, Bian Weimiff, Wu Xiaozu and Lai Zuhan (1994). "Flux pinning of stacking faults and dislocations in YBCO bulks." Physica C **235-240**: 2733-2734.

Zhang, W., Rupich, M. W., Schoop, U., Verebelyi, D. T., Thieme, C. L. H., Li, X., Kodenkandath, T., Huang, Y., Siegal, E., Buczek, D., Carter, W., Nguyen, N., Schreiber, J., Prasova, M., Lynch, J., Tucker, D., Fleshler, S. (2007). "Progress in AMSC scale-up of second generation HTS wire." Physica C: Superconductivity **463-465**: 505-509.

Zhou, Y. X., Ghalsasi, S., Rusakova, I., Salama, K. (2007). "Flux pinning in MOD YBCO films by chemical doping." Superconductor Science and Technology **20**(9): S147-S154.

Zwerger, S. S. a. W. (1997). "Ginzburg-Landau theory of superconductors with short coherence length." PHYSICAL REVIEW B **56**(14): 9004-9014.